INTRODUCTION INTO TRANSMISSION AND SCANNING TRANSMISSION ELECTRON MICROSCOPY

By FRANK KRUMEICH

Laboratory of Inorganic Chemistry
ETH Zürich
8093 Zürich, Switzerland

Email: krumeich@inorg.chem.ethz.ch

Website: www.microscopy.ethz.ch

1st version, May 2018

TABLE OF CONTENTS

1 INTRODUCTION

In 1931, *E. Ruska* and *M. Knoll* built the first transmission electron microscope (TEM) that consisted of two electromagnetic lenses.[1] Earlier calculations by *H. Busch* had revealed that such lenses are able to focus an electron beam. In spite of the small magnification of 17 times that the first TEM could achieve in two-steps, this observation provided the experimental proof that magnified images can indeed be formed with electrons using electromagnetic lenses in a similar way as with light in an optical microscope. This breakthrough got *Ruska* 55 years later the Nobel Prize in 1986. The TEM surpassed the resolution of the light microscope only a few years after its invention and several technical improvements led to a quick improvement of the achievable resolution. In particular, the optimization of the electron optics contributed to better imaging performance of the TEM. Around 1970, the best electron microscopes reached a resolution of about 3.5 Å. This resolution is sufficient to resolve columns of metal atoms in many oxide structures with octahedral frameworks like those of niobium oxides.[2] These structure characterizations can be regarded as the start of modern high-resolution TEM (HRTEM). A recent technical revolution was the calculation, construction and application of systems correcting the spherical aberration of the image forming lenses so that advanced aberration-corrected microscopes routinely reach sub-Å resolution today.[3,4]

Modern electron microscopy represents a collection of different techniques that offer unique possibilities to gain insights into structure, topology, morphology, and composition of materials. Various imaging and spectroscopic methods that utilize the multitude of electron-matter interactions are indispensable tools for the characterization of all types of structures with an increasingly higher resolution. New insights into many materials properties are gained by the unprecedented energy and spatial resolution provided by up-to-date analytical techniques with the ultimate limit being the analysis of a single atom.[5]

This introduction provides a qualitative explanation of the basics of several electron microscopy methods that are important for inorganic materials sciences. Other more specialized methods will not be discussed here, for example:

- Lorenz microscopy important the study of magnetic structures[6]
- electron holography used to image electric and magnetic fields[7], and

[1] E. Ruska. The development of the electron microscope and of electron microscopy. *Angew. Chem. Int. Ed.* **26 (**1987) 595-605.

[2] R. Gruehn, W. Mertin. High-resolution transmission electron microscopy re-examined as a tool in solid state chemistry. *Angew. Chem. Int. Ed.* **19** (1980) 505-520.

[3] H. Rose. Historical aspects of aberration correction. *J. Electron Microsc.* **58** (2009) 77–85.

[4] (a) S. J. Pennycook, M. Varela, C. J. D. Hetherington, A. I. Kirkland. Materials advances through aberration-corrected electron microscopy. *MRS Bulletin* **31** (2006) 36-43. (b) K. Urban. Is science prepared for atomic resolution electron microscopy? *Nature Mater.* **8** (2009) 260-262.

[5] D. A. Muller. Structure and bonding at the atomic scale by scanning transmission electron microscopy. *Nature Mater.* **8** (2009) 263-270.

[6] M. De Graef. Recent progress in Lorentz transmission electron microscopy. ESOMAT **2009** (2009) 01002, DOI:10.1051/esomat/200901002

[7] H. Lichte, P. Formanek,1 A. Lenk, M. Linck, C. Matzeck, M. Lehmann, P. Simon. Electron holography: applications to materials questions. *Annu. Rev. Mater. Res.* **37** (2007) 539–88.

- electron tomography to get a full three-dimensional picture of materials and biological structures[8].

This review starts with a short description of the operating principles of the different types of electron microscopes. The main part treats the electron-matter interactions in a qualitative way. Understanding these interactions is of course essential as they represent the basis of any electron microscopy application, used either in the various imaging or spectroscopic modes. Finally, the discussion of typical examples from various research projects taken from the author's own work will illustrate the power and versatility of the different electron microscopy methods.

This introduction into TEM and STEM is intended for students who start to work at an electron microscope themselves or who want to get a first idea what information which TEM or STEM method is capable to provide about the properties of particular materials. However, without an intense and time-consuming study of the underlying physics, the reader can gain only a limited depth of knowledge. Therefore, several textbooks are recommended here that are helpful to get a more comprehensive understanding of TEM and STEM in theory and practice.[9] References for more specific topics are quoted at the appropriate sites in the text.

[8] D. Schryvers, S. Cao, W. Tirry, H. Idrissi, S. Van Aert. Advanced three-dimensional electron microscopy techniques in the quest for better structural and functional materials. *Sci. Technol. Adv. Mater.* **14** (2013) 014206.

[9] (a) D. B. Williams, C. B. Carter. Transmission electron microscopy. Plenum Press, New York, 1996. (b) J. Thomas, T. Gemming, T. Analytical transmission electron microscopy - an introduction for operators. Springer, Berlin, 2014. (c) L. Reimer, H. Kohl. Transmission electron microscopy – Physics of image formation. 5th Edition, Springer, Berlin, 2008. (d) J. C. H. Spence. High-resolution electron microscopy. University Press, 3rd Edition, Oxford, 2003.

2 BASICS

2.1 PROPERTIES OF ELECTRONS

The electron *e* is an elementary particle that carries a negative charge. Although the phenomenon of electricity was basically already known in ancient Greece and numberless investigations had been made in the intermediate centuries, the electron was discovered not until 1897. While studying so-called cathode rays, which in fact are electron beams, *J. J. Thompson* (Nobel Prize 1906) discovered that these rays are negatively charged particles, which he called "corpuscles". Moreover, he found out that they are constituents of the atom and over 1000 times smaller than a hydrogen atom. Actually, the mass of the electron is approximately 1/1836 of that of a proton.

In 1924, *L. de Broglie* postulated the wave-particle dualism (Nobel Prize 1929). All moving matter has wave properties, with the wavelength λ related to the momentum *p*:

$$\lambda = h / p = h / mv$$

(*h* : Planck constant; *m* : mass; *v* : velocity)

This equation is of fundamental importance for electron microscopy because this means that accelerated electrons act not only as particles but as waves too. Consequently, the wavelength of moving electrons can be calculated from de Broglie's equation taking the energy E into account. An electron accelerated in an electric field *U* reaches an energy $E = eU$ which corresponds to a kinetic energy $E_{kin} = mv^2/2$. From this, the velocity *v* of the electron is derived:

$$v = (2eU/m_o)^{1/2}$$

(*U* : acceleration voltage; *e* : electron charge = -1.602 176 487 × 10^{-19} C; m_o : rest mass of the electron m_o = 9.109 x 10^{-31} kg).

It follows for the momentum p of the electron:

$$p = m_o v = (2m_o eU)^{1/2}$$

With this, an equation for the relation of wavelength and acceleration voltage *U* is derived from the de Broglie equation:

$$\lambda = h / \sqrt{2m_0 eU}$$

The values calculated for acceleration potentials *U* commonly used in TEM are listed in Table 1. It is important to note that these electrons move rather fast, and their speed approaches light velocity at high voltage. Therefore, a relativistic correction must be used for calculating the electron wavelength of electrons with $U \geq 100$ kV:

$$\lambda = h / \sqrt{2m_0 eU\,(1 + eU/2m_0 c^2)}$$

(speed of light in vacuum: c = 2.998 x 10^8 m/s)

U / kV	λ / pm	m x m_0	v / 10^8 m s^{-1}
100	3.70	1.20	1.64
200	2.51	1.39	2.09
300	1.97	1.59	2.33
400	1.64	1.78	2.48
1000	0.87	2.96	2.82

Table 1: Properties of electrons depending on the acceleration voltage *U*.

2.2 ELECTRON LENSES

The electron lens is a magnetic lens consisting of a coil of copper wire inside an iron cylinder (Figure 2.1a). An electric current through the coils creates a magnetic field that is rotationally symmetric but radially inhomogeneous: it is weak in the center of the lens but becomes stronger close to the bore in the iron cylinder. In this field an electron experiences the Lorentz force F:

$$\boldsymbol{F} = -e\,(\boldsymbol{E} + \boldsymbol{v} \times \boldsymbol{B})$$

with $|\boldsymbol{F}| = evBsin(\boldsymbol{v},\boldsymbol{B})$ for a magnetic lens

(*E*: strength of electric field, here: $E = 0$, *B*: strength of magnetic field; *e*/*v*: charge/velocity of electrons)

The overall effect of this magnetic field is that a beam of parallel electrons is focused into a spot (so-called *cross-over*) because electrons moving close to the lens center (optic axis) are less deflected than those passing the lens far from there. The focusing effect of such a magnetic lens increases with the magnetic field $\boldsymbol{B}$ that can be controlled by varying the current running through the coils. The force on moving electrons in the magnetic field is a vector product of the electron velocity $\boldsymbol{v}$ and the field strength $\boldsymbol{B}$. As a result, the force $\boldsymbol{F}$ is perpendicular to both, $\boldsymbol{v}$ and $\boldsymbol{B}$, leading to complicated helical trajectories of the electrons and to an image rotation (magnetic rotation). Apart from this effect, magnetic lenses influence electrons in a similar way as convex glass lenses do with light. Consequently, similar diagrams describe the respective ray paths and the vertical line through the centres of the lenses is called *optic axis* in both electron and light optics (Figure 2.1b).

Magnetic lenses have two different tasks in electron microscopes:

(i) They generate an electron beam with certain characteristics. The lenses in the condenser system forms either a parallel beam as required for TEM or a focussed beam for scanning techniques.

(ii) They form an image (objective lens) and magnify it (projective lenses) in a TEM.

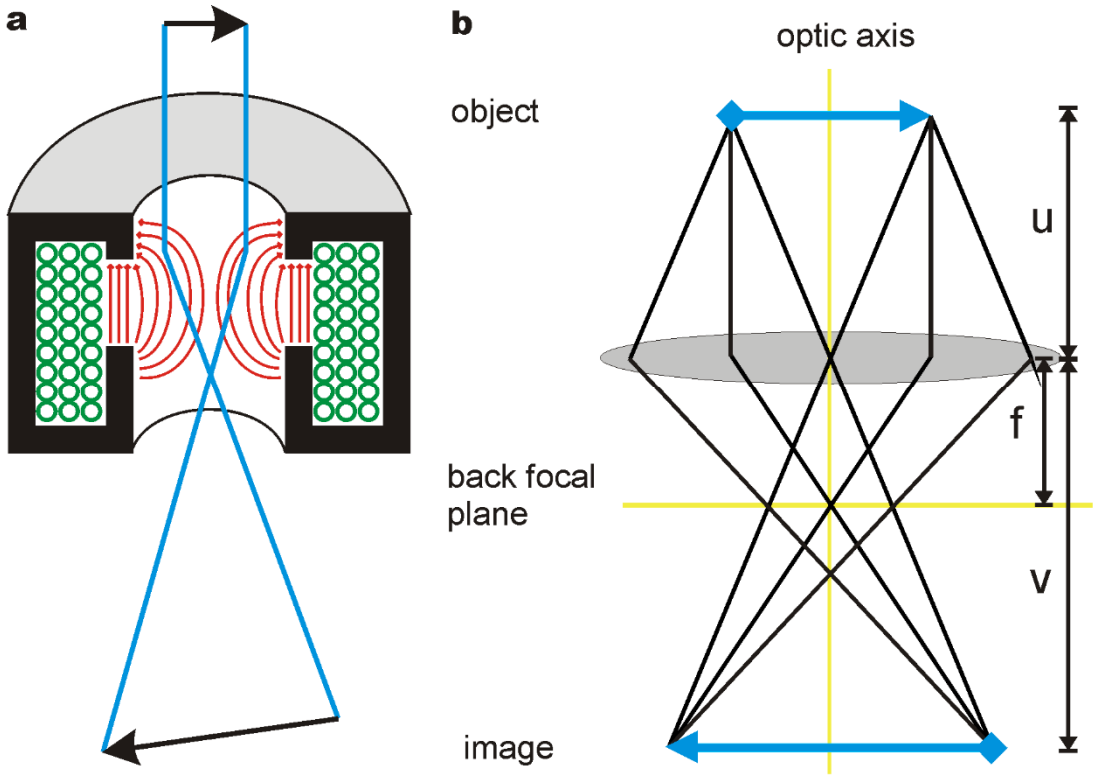

Figure 2.1: (a) Schematic cross-section of a magnetic lens. Copper wire (green) is coiled inside an iron cylinder (black). The rotationally symmetric but radially inhomogeneous magnetic field (red) focusses the electron beam (blue). Like in the light optical analogue with a convex glass lens (b), a magnified image of an object appears in the image plane but here it is rotated with respect to the object (magnetic rotation).

Similar to glass lenses used in light optics, the lens equation is valid:

$$1/u + 1/v = 1/f$$

(*f*: focal length; *u*: object distance; *v*: image distance).

Furthermore, magnetic lenses also suffer from several imperfections:

(i) **Astigmatism**: iron-based polepieces are not perfectly circular. This causes a distortion of the magnetic field leading to deviations from rotational symmetry. The resulting astigmatism of the objective lens can distort the image seriously and thus has to be corrected. Fortunately, astigmatism can easily be corrected by using quadrupole elements (so-called stigmators) which generate an additional electric field compensating the inhomogeneity of the magnetic field.

(ii) **Spherical aberration C_s**: off-axis electrons are deflected stronger than those close to the optic axis (Fig. 2.2b). The result is a spread focal point of the beam. In light microscopy, an appropriate concave lens compensates the spherical aberration of a convex lens. Although such dispersive lenses are not available in electron optics, a carefully designed corrector system, the so-called aberration corrector, can instead be applied to achieve a compensating dispersion effect analogous to a concave glass lens.

(iii) **Chromatic aberration C_c**: electrons of different wavelengths are deflected differently, leading to a focus spread as well (Fig. 2.2c). Ideally, electrons accelerated to a certain energy have the same wavelength. However, the energy spread and as a result the wavelength as well varies depending on the type of electron gun. The energy spread is high in a thermoionic

electron gun (ΔE > 1 eV) but smaller if a conventional field emitter is used as the electron source ($\Delta E \approx 0.6$ eV). An even smaller energy spread is achieved with cold field emitters ($\Delta E \approx 0.35$ eV) and monochromators ($\Delta E \approx 0.1$ eV).[10]

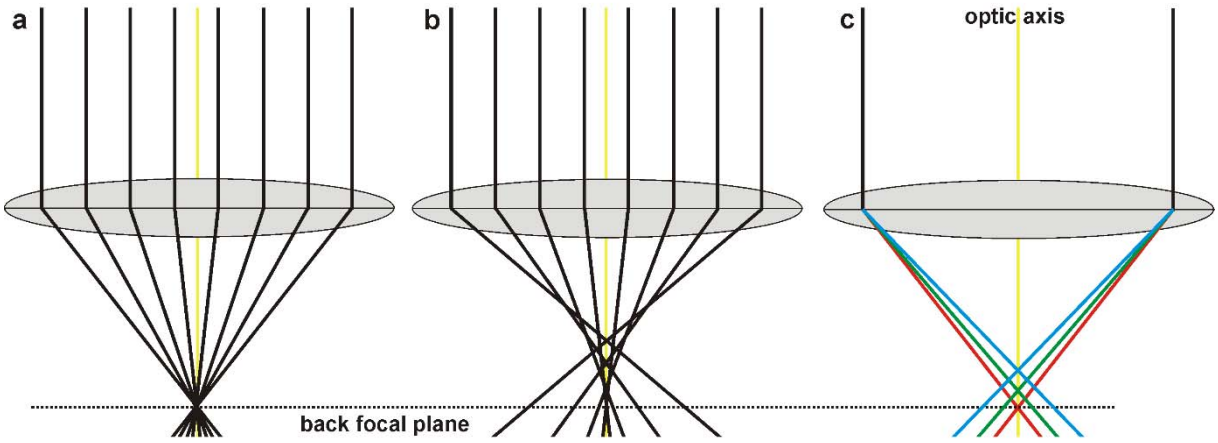

Figure 2.2: Ray diagrams of an ideal lens (a), of a lens with spherical aberration (b) and a lens with chromatic aberration.

2.3 TRANSMISSION ELECTRON MICROSCOPY (TEM)

Figure 2.3a shows a picture of a CM30 microscope, a typical standard TEM used in the 1990s. It is operated with an acceleration potential of 300 kV and a point resolution of ca. 2 Å is achieved. The microscope column with its various lenses and apertures is depicted in Figure 2.2b. In general, the electron gun is mounted at the top of a TEM and the generated electrons are then accelerated to a user-selected high energy, typically in the range 100 – 300 kV. To produce an electron beam, materials with a low work function for electron emission are utilized as the source. There are two different types of electron generation:

(i) In a thermionic electron gun, the filament (W fiber (Fig. 2.3c) or LaB_6 crystal (Fig. 2.3d)) is heated by an electric current, which provides the energy for the electron emission. The result is a broad, intense electron beam (Table 2).

(ii) The alternative is the field emission gun (FEG), in which electrons are extracted from a sharply pointed tip of a tungsten needle by applying an electric field (Fig. 2.3e). The generated electron beam has a higher coherence and can be focused into a small spot as needed for scanning transmission electron microscopy (STEM).

While propagated down the column, the electrons are focused into a particular beam by a condenser system that consists of different magnetic lenses and apertures (Fig. 2.3b). Today, most TEMs have the option to operate in STEM mode as well. This requires a flexible setting of the illumination conditions in order to generate either a parallel beam for TEM or a convergent beam with selected convergence angles for STEM.

[10] K. Kimoto. Practical aspects of monochromators developed for transmission electron microscopy. *Microscopy* **63** (2014) 337–344.

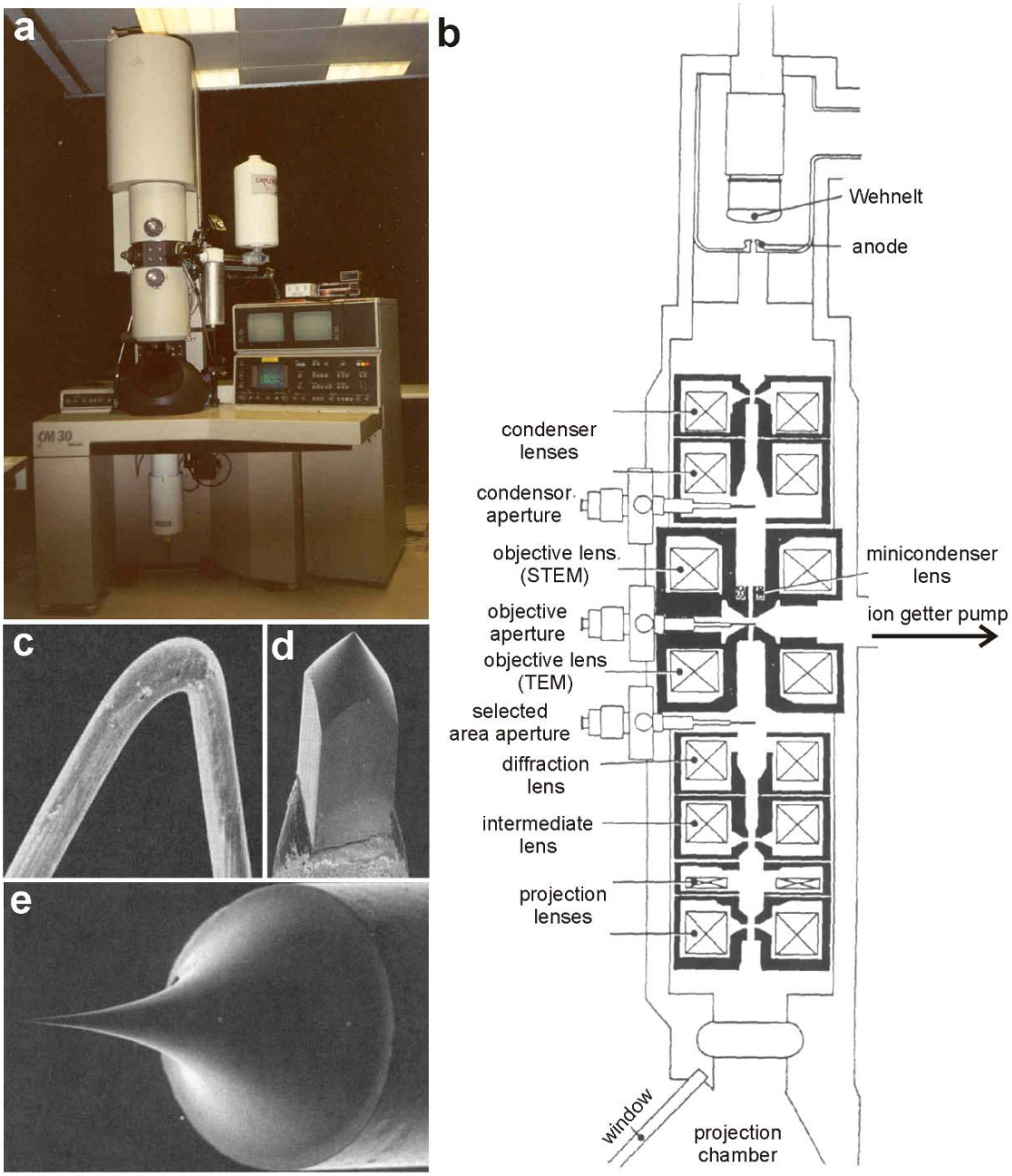

Figure 2.3: (a) Photo of a CM30 microscope (Philips). (b) Scheme showing the position of lenses and apertures in the CM30. (c)-(e) Different types of cathodes: W fibre (c), LaB_6 crystal (d) and W tip of a FEG (e).

The electron beam then interacts with the specimen. Most microscopes have so-called side-entry goniometers by which the sample holders are inserted into the high vacuum of the column. Besides the standard single and double tilt holders, special sample holders enable one to perform in-situ heating, cooling and straining experiments. It is often necessary to study a material along a certain direction, e.g. crystals along a crystallographic zone axis. To achieve a certain orientation of an arbitrarily oriented sample, it is tilted in two perpendicular directions using a double tilt holder while observing the electron diffraction pattern. For this, it is certainly an advantage to have large tilt angles, but the trade-off is a reduced resolution that is better for small polepiece gaps limiting the space for tilting.

The objective lens is positioned below the sample and represents the most important lens in the microscope since it generates the first intermediate image as well as the first diffraction pattern (Fig. 2.4). The quality of the image formed by the objective lens indeed determines the resolution of the whole microscope. The diffraction lens system located below the objective lens can be focussed either on the image or on the diffraction pattern and thereby determines which of them is further magnified by the projective lenses. The diffraction lens allows one to switch between imaging and diffraction mode just by pressing a knob. The possibility to work almost simultaneously in real space and in reciprocal space at the same area of a specimen makes TEM an outstanding tool for materials characterization.

	W (Fig 2.3c)	**LaB_6** (Fig 2.3d)	**FEG** (Fig 2.3e)
Work function / eV	4.5	2.4	4.5
Temperature / K	2700	2000	(300-)1800
Energy spread / eV	3-4	1.5-3	0.4-1.5
Source size / nm	30000	5000	3-20
Maximum current / nA	1000	500	(30-)300
Brightness / $A/m^2 sr$	10^9	$5 \cdot 10^{10}$	10^{13}
Lifetime / h	100	500	>1000

Table 2: Characteristics of different electron guns.

Moreover, an aperture (objective aperture) can be inserted in the back focal plane of the objective lens to select one or more beams in diffraction mode (Fig. 2.5). An aperture is just a metal plate with holes; only the electrons hitting a hole pass the aperture then whereas others are completely absorbed by the metal. The selected beams then built up an image with particular information (Fig. 2.5). If only the beam on the optic axis is allowed to pass the aperture, a bright-field TEM image (BF-TEM) is formed. The aperture can be shifted to select one or more diffracted beams resulting in a dark-field (DF) TEM image. To ensure a high image quality, this aperture has to be on the optic axis of the microscope. For this purpose, the electron beam is tilted before the sample in such a way that the selected diffracted beam passes through the aperture that stays on the optic axis. If a large aperture is selected, the direct beam as well as several diffracted beams are collected so that they interfere with each other in the imaging plane. This is the set-up used for high-resolution TEM (HRTEM). Another aperture, the selected area aperture, placed in the plane of the first intermediate image enables one to choose the specimen region of which a selected area electron diffraction (SAED) pattern is obtained (Figs. 2.3b and 2.4).

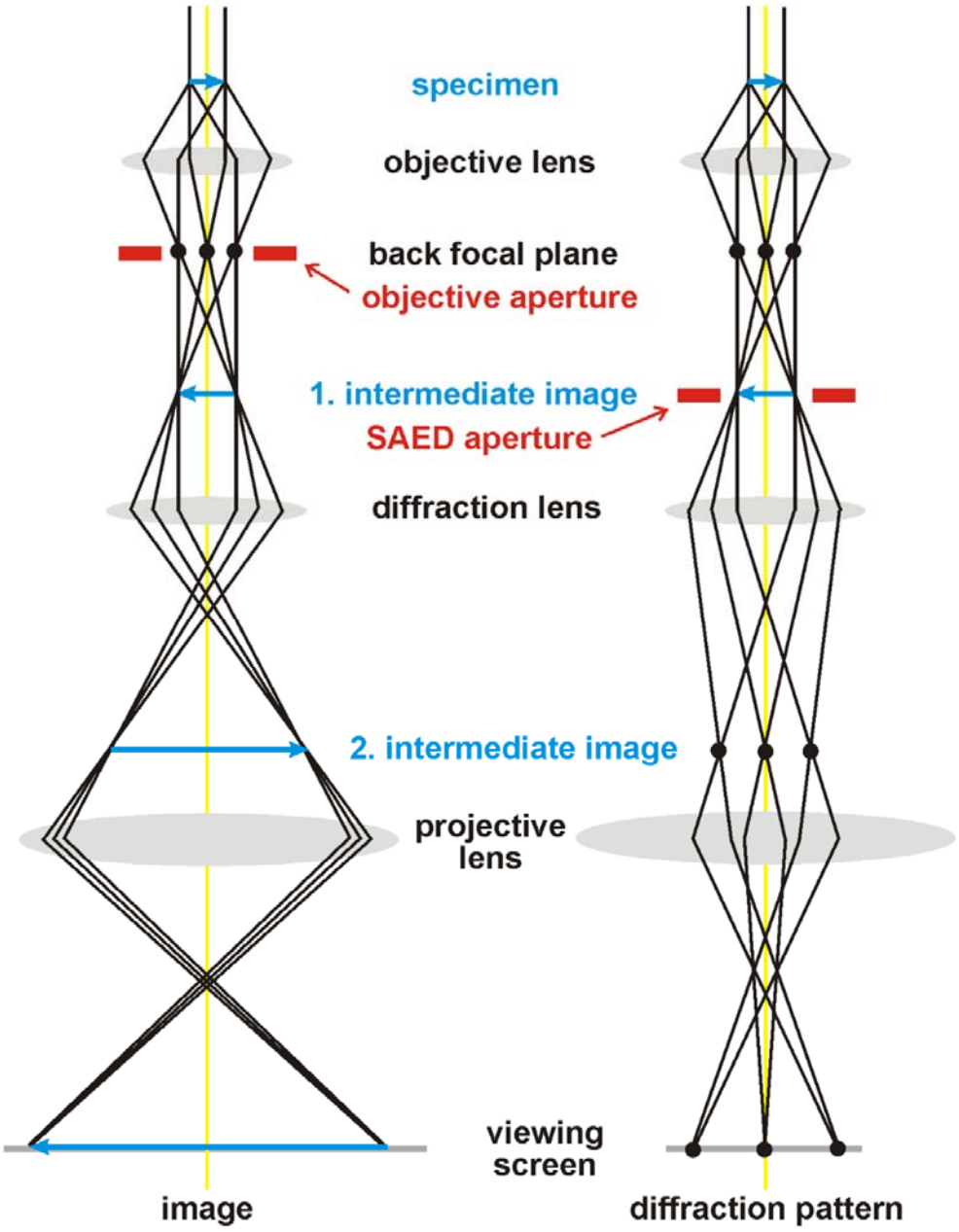

Figure 2.4: Scheme showing the ray paths in imaging mode (left) and diffraction mode (right) of a TEM. The first lens below the objective lens, called diffraction (or sometimes intermediate) lens, is either focused onto the first intermediate image (in imaging mode) or onto the back focal plane (in diffraction mode). An image or a diffraction pattern appears in the second intermediate image plane and further magnified on the viewing screen.

The final image or diffraction pattern can directly be observed either on the viewing screen in the projection chamber or on a TV or CCD camera mounted below the microscope column. Slow-scan CCD or CMOS cameras are used to record the images.

Because of the strong interaction of electrons with any matter, unwanted scattering with gas particles diminishes the instrument performance. Thus, high vacuum must be maintained in the microscope column. The required vacuum system typically comprises a rotary pump (pre-vacuum pump), a diffusion pump, and one or more ion getter pumps (Fig. 2.3b).

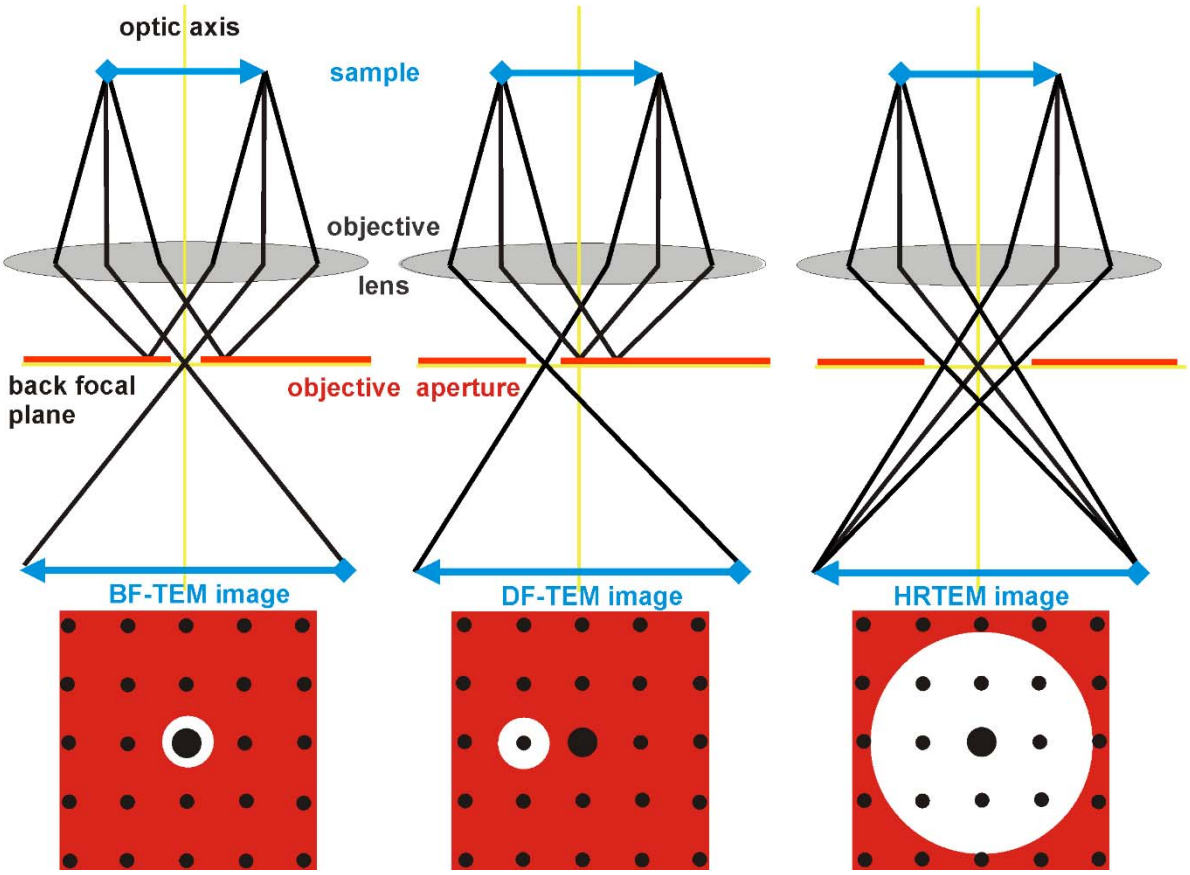

Figure 2.5: TEM imaging modes: scheme of the ray paths from the object (sample) to the first intermediate image. The position of the objective aperture (red) in the electron diffraction pattern (black dots) formed in the back focal plane of the objective aperture is shown in side view (top) and projected along the optic axis.

2.4 Scanning Transmission Electron Microscopy (STEM)

While TEM works with a parallel illumination, STEM like scanning electron microscopy (SEM) uses a tiny, convergent electron beam. The beam is scanned across a defined specimen area and generated signals are recorded by selected detectors spot-by-spot, forming an image on a screen pixel by pixel.

Three main types of detectors are used to obtain STEM images (Figure 2.6):

1. **BF detector:** the bright field detector is placed on the optic axis of the microscope. It detects the intensity in the direct beam after passing a point on the specimen and the image provides information analogous to BF-TEM.

2. **ADF detector**: the annular dark field detector is a ring-shaped semiconductor device covering collection angles in the range of ca. 10-50 mrad). The ADF detector uses electrons scattered or diffracted into small angles for image formation and therefore is similar to the DF-TEM mode. The measured contrast mainly results from electrons diffracted in crystalline areas but is superimposed by incoherent scattering (see below).

3. **HAADF detector**: the high-angle annular dark field detector is also a semiconductor disk with a hole, but the inner diameter (> 50 mrad) is much larger than in the ADF detector. Thus,

it detects electrons that are scattered into high angles arising almost exclusively from incoherent scattering events. Thus, Rutherford scattering generates the image contrast and thereby atomic number (Z) contrast is achieved (see below).

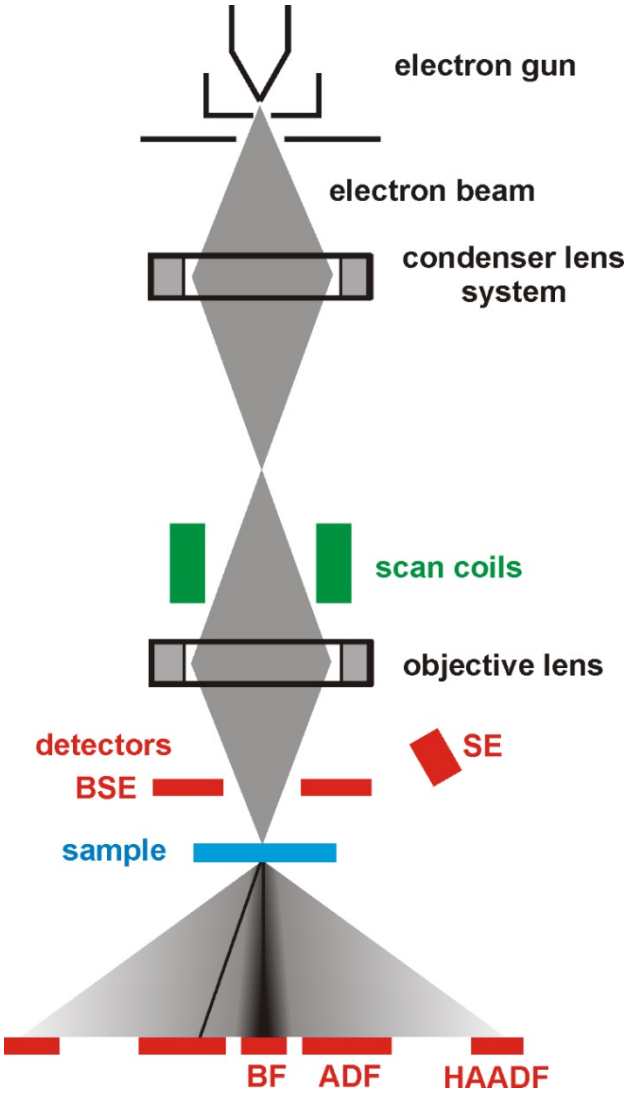

Figure 2.6: Scheme of a scanning (transmission) electron microscope showing the ray path and the detector arrangement. In a conventional SEM, secondary electrons (SE) and back-scattered electrons (BSE) are collected for image formation on the upper side of the sample. For STEM, detectors are installed below the thin sample: BF: bright field detector; (HA)ADF: (high angle) annular dark field detector). The intensity distribution of the electrons scattered by the sample is indicated by the different grey values. Most electrons pass a thin sample without any interaction or are scattered into small angles only. Diffracted beams (black line symbolizes an example) meet the ADF detector.

In addition to these detectors below the specimen, there is the option to install a detector for secondary electron (SE) and/or back-scattered electrons (BSE) above the sample like in a SEM microscope and to obtain supplementary morphological and topological information.[11] An example is reproduced in Fig. 2.7: gold nanoparticles are clearly visible in both HAADF- and

[11] F. Krumeich, E. Müller, R. A. Wepf, R. Nesper. Characterization of Catalysts in an Aberration-Corrected Scanning Transmission Electron Microscope. *J. Phys. Chem C* **115 (**2011) 1080-1083.

SE-STEM images. The SE-STEM image reveals that most particles are located on the surface of the TiO_2 crystals. In fact, the boundaries between SEM and STEM are disappearing in up-to-date instruments: besides SE and BSE imaging in the STEM, electron transparent samples can be investigated in a SEM by using special holders that produce BF- and ADF-STEM images at low voltages ($U_{acc} \leq 30$ kV) in addition to the conventional SE and BSE images.

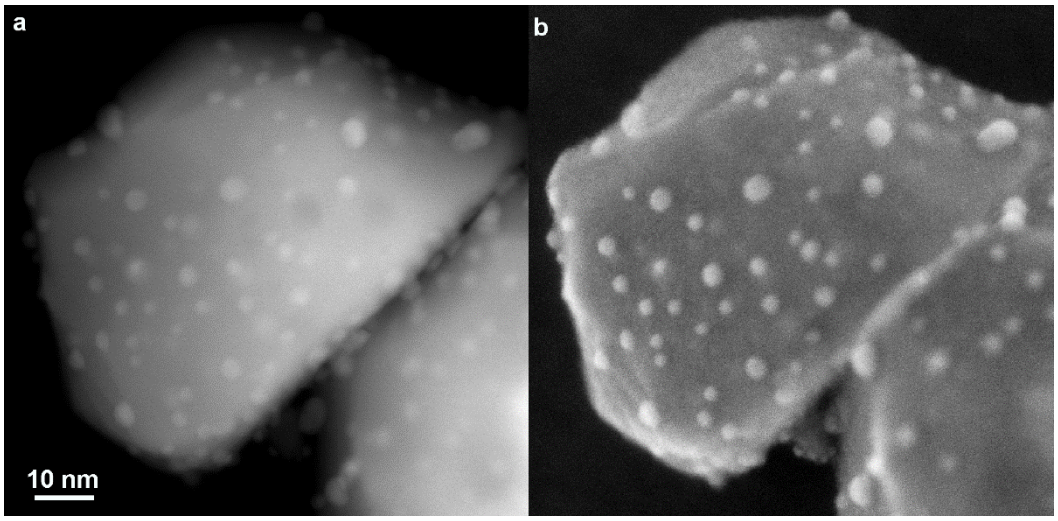

Figure 2.7: (a) HAADF-STEM and (b) SE-STEM image of Au-NPs on TiO_2.

Many modern microscopes allow the operation in TEM and STEM mode. This requires two optimized objectives lenses what technically is often solved by a so-called twin lens system (Fig. 2.3b):

(i) STEM mode. The last lens of the condenser system is the probe forming lens, i.e. it focusses the electron beam on the sample. The achievable resolution is determined by the minimal beam diameter d and depends on the quality of the lens: $d = 0.41\ C_s^{1/4}\lambda^{3/4}$.

(ii) TEM mode. The first lens below the sample forms the first intermediate image. Also here, the resolution Δx depends on the spherical aberration of the lens: $\Delta x = 0.66\ C_s^{1/4}\lambda^{3/4}$.

To achieve a better resolution, one way is to decrease the wavelength λ, i.e. to increase the acceleration voltage U. Following this way, a resolution of ca. 1 Å was reached in the 1990ies on megavolt TEMs.[12] However, such TEMs are expensive and the highly energetic electron beam destroys many materials. Therefore, TEM at medium voltage (U_{acc} = 200–300 kV) has become more popular and found widespread application. Improvements of the electron optics, in particular the reduction of the spherical aberration C_s of the objective lens, gives rise to achievable point resolutions well below 2 Å so that such microscopes are standard since ca. 1990. However, the long desired jump into the sub-Å regime has necessitated more effort from the technical side, as the correction of the spherical aberration is indispensable.

[12] F. Phillipp, R. Höschen, M. Osaki, G. Möbus, M. Rühle. New high-voltage atomic resolution microscope approaching 1 Å point resolution installed in Stuttgart. *Ultramicroscopy* **56** (1994) 1-10.

2.5 Aberration-corrected TEM and STEM

The correction of the spherical aberration C_s of magnetic lenses (cf. Fig. 2.8a) was experimentally achieved around the year 2000 based on a corrector design proposed by H. Rose.[13] This carefully designed so-called aberration corrector consists of two hexapols and two transfer lenses that can indeed achieve a dispersion effect compensating for the spherical aberration of the following lens. This occurs in an analogous way as in light optics where a concave glass lens can neutralize the spherical aberration of a focussing convex lens (Fig. 2.8). With the correction of the C_s aberration of the objective lens, the barrier of 1 Å was quickly surpassed and resolutions down to ca. 0.5 Å had been reached in both microscope modes TEM and STEM. Microscopes with such high resolution capability are widely available today, which has opened new fascinating perspectives to characterize materials with unprecedented precession. Moreover, it is of outmost importance that aberration-corrected TEMs allow structural investigations without the disturbing effect of the delocalisation of information as caused by the spherical aberration. Especially, the study of interface structures has become more straightforward. Aberration-corrected TEM and STEM microscopes are now available world-wide and frequently applied for the precise characterization of defects as well as of modulated and disordered structures with highest possible resolution and with minimized information delocalisation.[14]

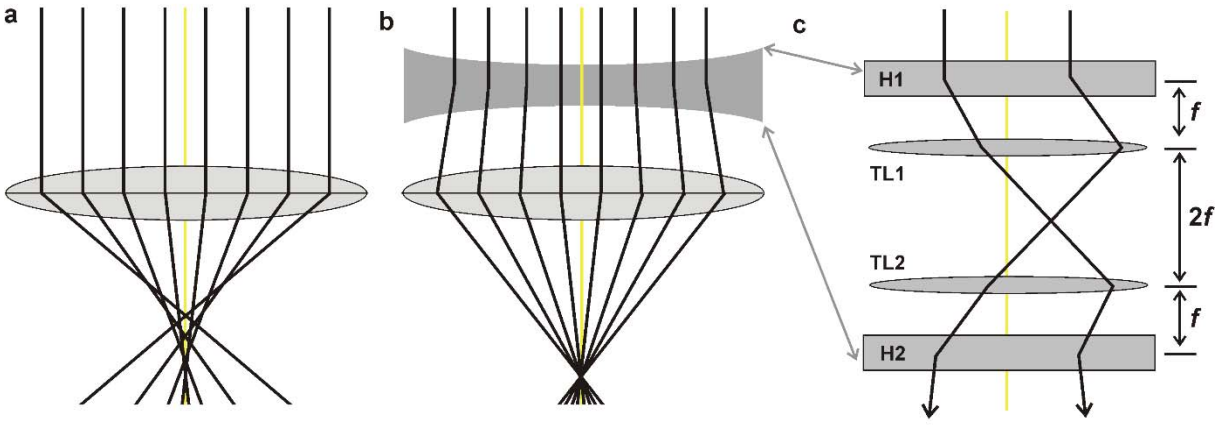

Figure 2.8. In light optics, the spherical aberration (a) is corrected by a dispersive lens (b). In electron optics, hexapole-based corrector are applicable to achieve a dispersion of an incoming parallel electron beam (c). The corrector consists of two equally excited hexapole elements (H1, H2) and two round transfer lenses (TL1, TL2).

As the resolution of a STEM is determined by the diameter of the focussed electron beam, the correction of the spherical aberration of the probe-forming lens leads to substantial improvements of the imaging properties. Forming an electron beam with a diameter of less than

[13] M. Haider, H. Rose, S. Uhlemann, E. Schwan, B. Kabius, K. Urban. Towards 0.1 nm resolution with the first spherically corrected transmission electron microscope. *J. Electron Microsc.* **47** (1998) 395–405.

[14] (a) G. Van Tendeloo, J. Hadermann, A. M. Abakumovab, E. V. Antipov. Advanced electron microscopy and its possibilities to solve complex structures: application to transition metal oxides. *J. Mater. Chem.* **19** (2009) 2660–2670. (b) K. Urban, C.-L. Jia, L. Houben, M. Lentzen, S.-B. Mi, K. Tillmann. Negative spherical aberration ultrahigh-resolution imaging in corrected transmission electron microscopy. *Phil. Trans. R. Soc. A* **367** (2009) 3735–3753.

0.1 nm gives access to the sub-Angstrom regime as it is achieved in aberration-corrected TEMs as well.

Another important application of C_s correction are TEM investigations at lower voltages than those normally applied up to now ($U_{acc} \geq 100$ kV). For example, the knock-on damage of graphene happens at an energy of about 90 kV. Today many carbon structures, in particular variants of graphene, are therefore observed at low voltages ($U_{acc} \leq 80$ kV) to avoid such unwanted effects.[15]

The availability of a precisely focussed electron beam in probe-corrected STEM improves not only the resolution of imaging but also that of analytical studies: HAADF-STEM coupled with EELS and EDXS is an outstanding tool to image and chemically characterize small areas down to small clusters and even single atoms. Technique and applications of aberration correction are treated in excellent textbooks.[16]

[15] (a) O. L.Krivanek, N. Dellby, M. F. Murfitt, M. F. Chisholm, T. J. Pennycook, K. Suenaga, V. Nicolosi, Gentle STEM: ADF imaging and EELS at low primary energies. *Ultramicroscopy* **110** (2010) 935-945. (b) S. Kurasch, J. Kotakoski, O. Lehtinen, V. Skakalova, J. H. Smet, C. Krill, A. V. Krasheninnikov, U. Kaiser. Atom-by-atom observation of grain boundary migration in graphene. *Nano Lett.* **12** (2012) 3168–3173.

[16] (a) S. J. Pennycook, P. D. Nellist. Scanning transmission electron microscopy. Springer, New York, 2011. (b) R. Brydson. Aberration-corrected analytical transmission electron microscopy. John Wiley and Sons, Ltd., Chichester, 2011. (c) R. Erni, Aberration-corrected imaging in transmission electron microscopy. Imperial College Press, 2nd Ed., London, 2015.

3 ELECTRON-MATTER INTERACTIONS AND THEIR APPLICATIONS

The many different electron microscopy methods offer outstanding possibilities to characterize a material's structure, topology, morphology, and composition. The versatility of information that is obtainable is based on the multitude of signals that are caused by the various interaction of electrons with a matter (Fig. 3.1). The understanding of these interactions represents an essential requirement to understand the results obtained by the various electron microscopy methods. Electron-matter interactions are classified into two types, namely elastic and inelastic interactions. Some basic physics and applications of the different interactions in electron microscopy will be discussed in the following.

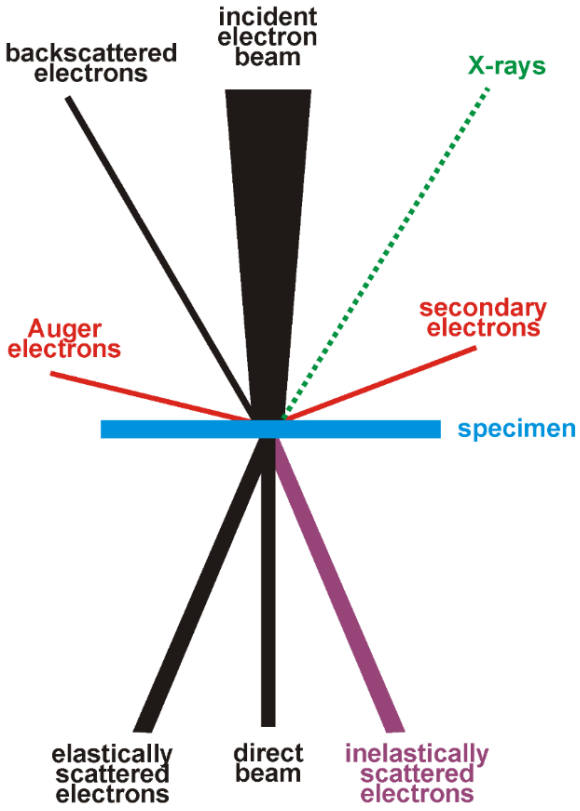

Figure 3.1: Scheme showing the most important electron-matter interactions arising during the interaction of an electron beam with a specimen. If the sample thickness is small enough to allow at least a part of the electrons to pass through, then certain signals below the sample are observable.

3.1 Elastic Interactions

During an elastic electron-matter interaction, no energy transfer from the energy-rich incoming electron to the sample happens. Consequently, the electron still carries its original energy ($E_{el} = E_o$) after passing the sample. If the electron goes through the sample without any interaction at all, this of course is the case as well. These electrons contribute to the direct beam which contains the electrons that pass the sample in direction of the incident beam (Fig. 3.1).

Elastic scattering happens also if electrons are deflected from their path by Coulomb interaction with the nucleus of an atom in the sample. By this process, the scattered electron loses no measurable amount of energy.

3.1.1 Incoherent Scattering

For the description of the elastic scattering of an electron by an atom, it is sufficient to regard it as a negatively charged particle and neglect its wave properties.

An electron penetrating into the electron cloud of an atom is attracted by the positive potential of the nucleus (electrostatic or Coulombic interaction), and its path is deflected towards the core as a result (Fig. 3.2a). The Coulombic force F responsible for such an interaction is defined as:

$$F = Q_1 Q_2 / 4\pi \varepsilon_o r^2$$

(r: distance between the charges Q_1 and Q_2; ε_o : dielectric constant).

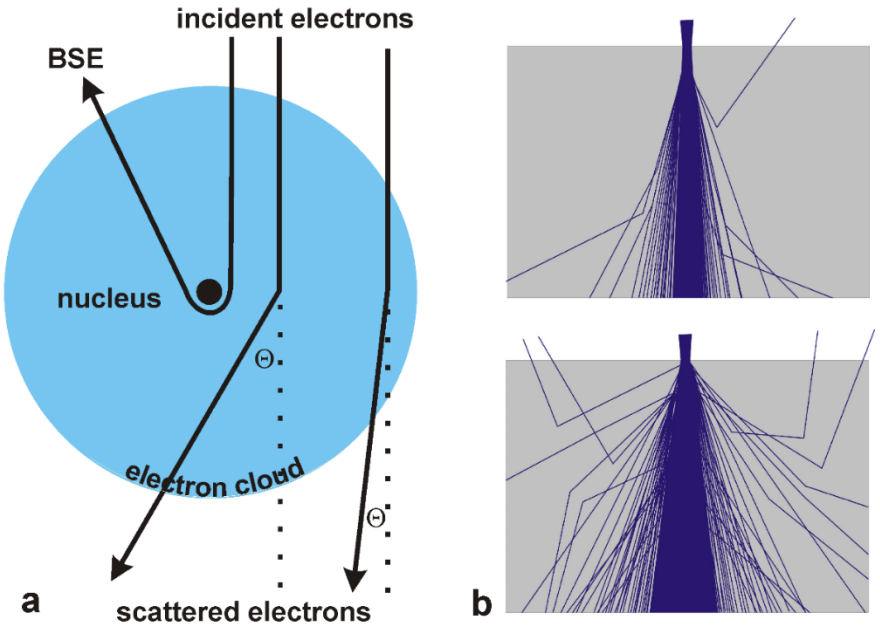

Figure 3.2: (a) Scheme demonstrating the scattering of an electron inside the electron cloud of an atom. Electrons passing the core in a small distance may be scattered into high angles or even backwards (BSE). (b) Interaction of an electron beam with a low Z (top) and high Z material (bottom). Most electron are scattered forward. Beam broadening and the likelihood of scattering events into high angles or backwards increase with higher Z.

The closer the electron comes to the nucleus, i.e. the smaller r, the larger is F and consequently the scattering angle. In rare cases, electrons can even be turned backwards, generating so-called back-scattered electrons (BSE). These electrostatic electron-matter interactions can be treated as elastic. Note that for an accurate description of this process, however, phonon scattering and thermal diffuse scattering (TDS) must be considered which are in fact inelastic effects but result in minute energy losses of a few meV only that cannot be measured.

Because of its dependence on the charge, the force F, with which an electron is attracted by the nucleus, is stronger if there are more positives charges, i.e. more protons. Thus, the Coulomb

force increases with increasing atomic number Z. If electrons scattering into high angles or even backwards are collected for image formation, the brightness increases with Z (Z contrast) giving rise to chemical information (Fig. 3.2b).

The Coulomb interaction of electrons with matter is strong and consequently multiple scattering of electrons passing a sample happens frequently. When an electron passes through a specimen, it may be scattered not at all, once (single scattering), several times (plural scattering), or even many times (multiple scattering). Although electron scattering occurs most likely in the forward direction, there is a small probability for backscattering (Fig. 3.2). The statistical prediction of electron-matter interactions requires the probability laws as provided by quantum mechanics. The concept of the scattering cross-section expresses the likelihood of an interaction. It is based on the simple model of an effective interaction area: if an electron passes through this area, an interaction will certainly occur. Dividing such an atomic cross-section by the atom's actual area gives a probability for an interaction event. Therefore, the likelihood for a certain interaction increases with increasing cross-section. Note that each type of possible electron-matter interaction for a given electron beam energy has a characteristic cross-section.

The angular distribution of electrons scattered by an atom is described by the differential cross-section $d\sigma/d\Omega$. Electrons are scattered by an angle Θ and collected within a solid angle Ω (Fig. 3.3a). If the scattering angle Θ increases, the cross-section σ decreases so that scattering into high angles occurs rarely. The differential cross-section is important since it is the measured quantity in annular dark field STEM (see 2.4). If electron scattered to large scattering angles are measured, the intensity scales with the atomic number Z^2. Owing to the high contrast of this method, small clusters and even single atoms of a heavy metal on a light support can be observed by HAADF-STEM. An example are clusters and single atoms of Pt that appear with bright contrast in the HAADF-STEM image (Fig. 3.3b). Z contrast imaging is achieved not only in HAADF-STEM but also in SEM by imaging with back-scattered electrons.

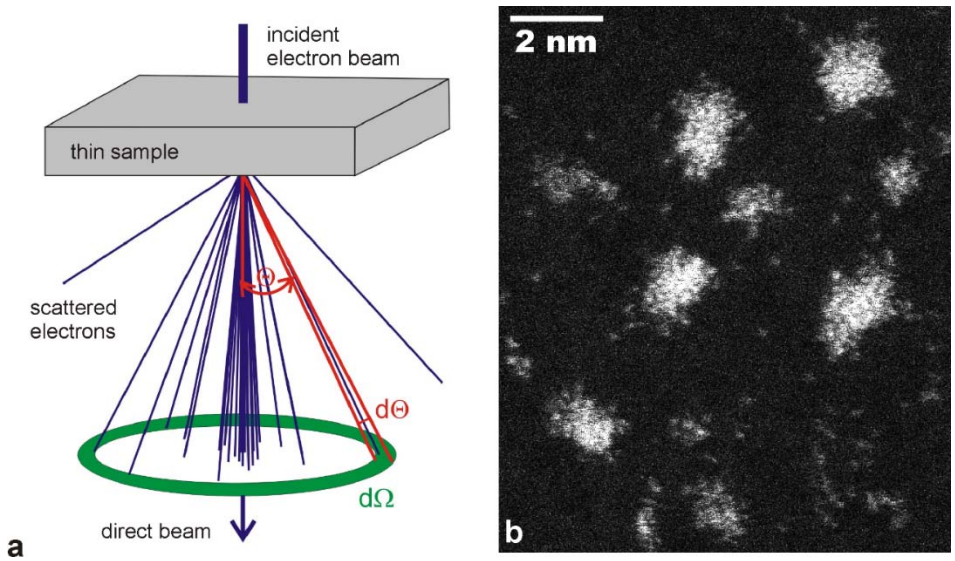

Figure 3.3: (a) Schemes of annular distribution of electron scattering after passing through a thin sample. The scattering semiangle Θ, its incremental changes $d\Theta$, and the solid angle Ω (respectively its incremental changes $d\Omega$) of their collection are used to describe this process. Annular detectors in STEM measure the amount of electrons scattered in $d\Omega$. (b) HAADF-STEM images of Pt clusters and single atoms on carbon.

3.1.2 Coherent Scattering (Diffraction)

As described above. incoherent scattering is the main effect if the scattering centres are arranged in an irregular way like in amorphous compounds. A part of the electrons in the incoming, largely coherent beam is thereby deflected with the likelihood in decreasing with increasing scattering angle. All atoms act as scattering centres that turn a part of the incoming electrons away from their direct paths due to the electrostatic interaction of the negatively charged electrons with the nucleus (Fig. 3.2a). If the scattering centres are located on a lattice, i.e. if the sample is crystalline, then coherent scattering takes place: constructive interference of the scattered electron waves occurs in certain directions and thereby diffracted beams are generated (Bragg diffraction).

The Bragg equation describes the relation between diffraction angle, electron wavelength and interplanar distance (Fig. 3.4). This simplified model treats the diffraction of an incoming electron wave as a reflection of the beams by the equidistant lattice planes. This consideration results in a general equation for diffraction that is valid not only for electrons but for X-rays and neutrons as well. Two incident electron waves, which are in phase with each other (left side in Fig. 3.4), are reflected by the lattice planes. After this, constructive interference occurs if in phase again (right side). The condition for this is that the distance, which the wave with the longer path travels, is an integer multiple of the electron wavelength λ_{el}. The path length also depends on the incident angle Θ and the distance between the lattice planes d. It is equal to two times $d \bullet \sin\Theta$. Because this value must be a multiple of λ_{el}, it follows:

$$2d \sin\Theta = n \lambda$$

From this Bragg equation, values for the diffraction angles can be calculated. For U = 300 kV, the wavelength is λ = 0.00197 nm. For a typical d-value of 0.2 nm, an angle Θ = 0.28° results. As a consequence of the small wavelength of the high-energy electrons used in TEM, the diffraction angles observed in electron diffraction are quite small and typically are in the range $0° < \Theta < 1°$.

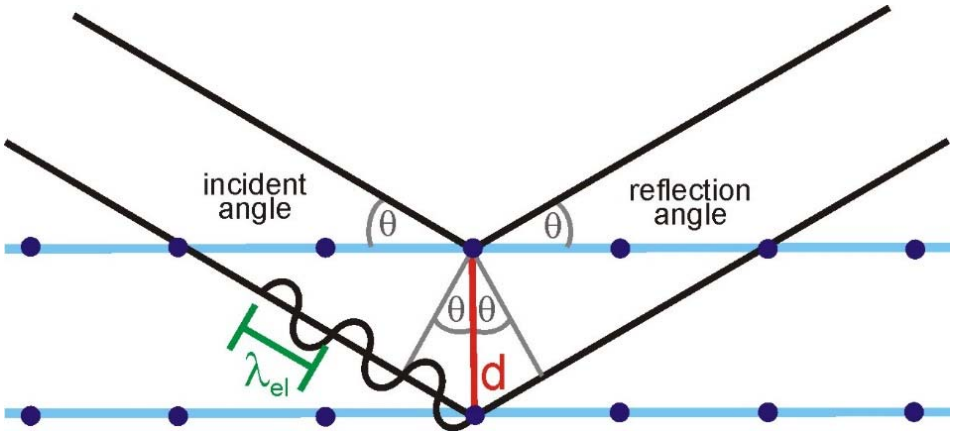

Figure 3.4: Reflection of two parallel electron beams by a set of two parallel lattice planes representing a crystal structure resulting in constructive interference.

3.1.3 Electron Diffraction

Since the diffraction angles are small ($\Theta < 1°$), the reflecting lattice planes are almost parallel to the incoming beam of ideally parallel electrons (Fig. 3.5a). If a crystal is oriented along a low-indexed zone axis with respect to the electron beam, then the beam is on a zone axis, i.e. at the intersection of two or more sets of parallel lattice planes (Fig. 3.5b). This gives rise to the electron diffraction pattern of a single crystal with the reflections appearing on well-defined points of reciprocal space. Note that every lattice plane generates two spots in the diffraction pattern. Mathematically, this operation corresponds to a Fourier transform of the crystal potential. The spot arrays are characteristic for the crystal structure and symmetry, the distances of the spots provide information about its lattice parameters. As an example, the electron diffraction pattern of a single crystal silicon orientated along [011] is shown (Fig. 3.5c). Note that the reflection (100) is not observed due to the face-centered unit cell of Si. In general, such extinctions give useful crystallographic information about the symmetry of the unit cell, e.g. the presence of centering and glide-planes.[17]

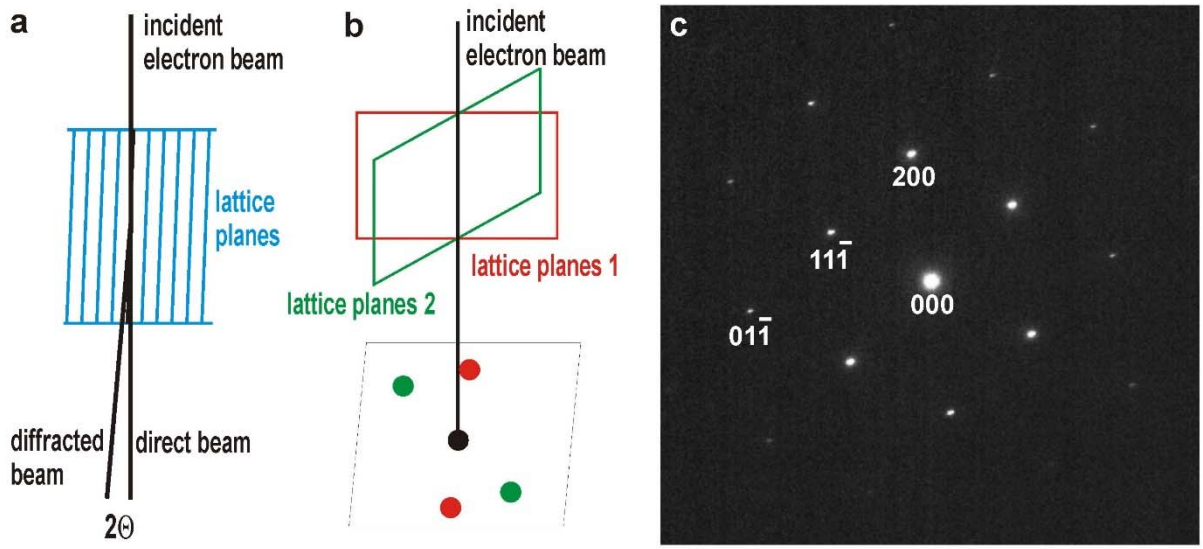

Figure 3.5: (a) Diffraction of an electron beam by a schematically depicted crystal (lines represent a set of parallel equidistant lattice planes). (b) Diffraction pattern generated by the diffraction of the electron beam at two sets of parallel lattice planes (represented by one plane). (c) Selected area electron diffraction (SAED) patterns of single crystal of Si in [011] orientation. Some indices are assigned to the corresponding diffraction spots.

Different types of selected area electron diffraction (SAED) patterns are observed depending on the size of the investigated crystallites. Besides diffraction patterns of single crystal consisting of spot arrays, ring patterns occur for polycrystalline samples (Fig. 3.6) Here, the superposition of the diffraction patterns of many small micro- or even nanometer-sized crystallites leads to diffraction rings. All diffracting lattice planes with the same interplanar distance give rise to spots with the same distance to the origin of reciprocal space and, if there are many of them, they form such a ring. The ring diameters correspond to d-values that can be attributed to certain lattice planes and accordingly assigned with indices. The high symmetry

[17] J. P. Morniroli, J. W. Steeds. Microdiffraction as a tool for crystal structure identification and determination. *Ultramicroscopy* **45** (1992) 219-239.

of the face-centered cubic structure of platinum allows only a few reflections (hkl) to appear in the diffraction pattern (Fig. 3.6b).

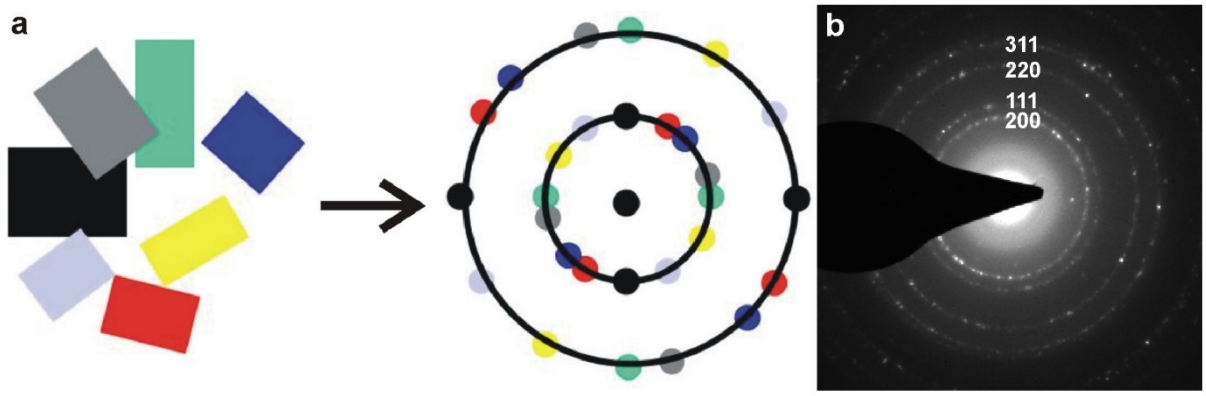

Figure 3.6: (a) Generation of rings by superposition of the diffraction spots of many individual crystals. (b) SAED patterns polycrystalline platinum. Indices are assigned to the diffraction rings.

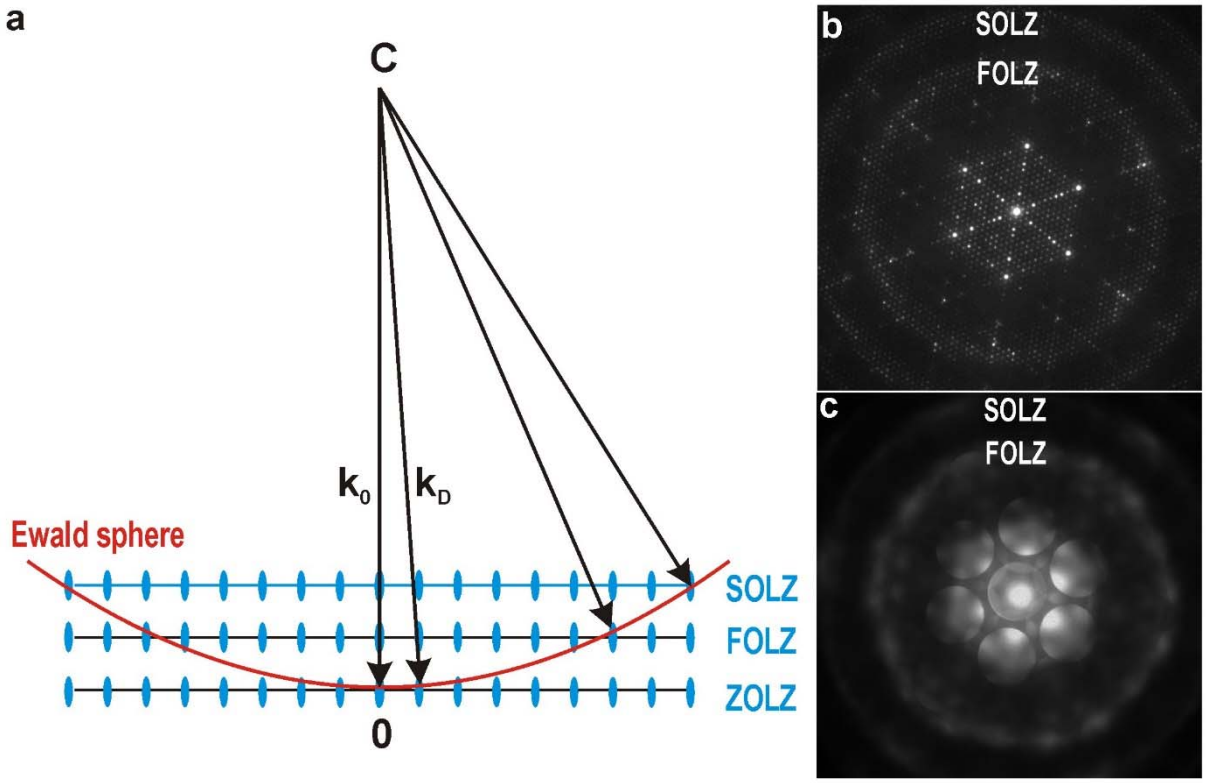

Figure 3.7: (a) Ewald sphere construction (point 0: origin of reciprocal lattice, $\mathbf{k_0}$: wave vector of the incident wave, $\mathbf{k_D}$: wave vector of a diffracted wave, ZOLZ (FOLZ, SOLZ): Zero (First, Second) order Laue zone). (b) SAED and (c) CBED of a cubic AlCuTa phase along [111] showing FOLZ and SOLZ rings.

Alternatively, a description of diffraction can be made in reciprocal space by the Ewald sphere construction (Fig. 3.7a). A sphere with radius $1/\lambda$ is drawn so that it contains the origin of the reciprocal lattice. Then, for each reciprocal lattice point that is located on the Ewald sphere of reflection, the Bragg condition is satisfied and a diffraction spot arises. The radius of the Ewald sphere ($1/\lambda$) is quite large due to the small wavelength of electrons (e.g., $\lambda = 1.97$ pm for 300 keV electrons). Furthermore, the lattice points in the reciprocal lattice of thin samples

are elongated so that the Ewald sphere intersects several of these so-called relrods even if the Bragg condition is not exactly fulfilled (excitation error) and as the result many reflections appear simultaneously. Thus, electron diffraction patterns correspond to 2D cuts of the reciprocal lattice. If the interplanar distance in direction of observation is small in reciprocal space, then the Ewald sphere intersects also higher order Laue zones (HOLZ) that are then observed as well. The example shown in Figure 3.7b is the [111] direction of an intermetallic phase with an extraordinary large unit cell (cubic AlCuTa with $a \approx 71.5$ Å).[18] Besides SAED obtained with a parallel electron beam (*cf.* Fig. 2.4), a convergent beam can be used to get additional information about crystal symmetry and higher order Laue zones (convergent beam electron diffraction, CBED). Such CBED patterns show diffraction disks instead of spots in the SAED (Fig. 3.7c).

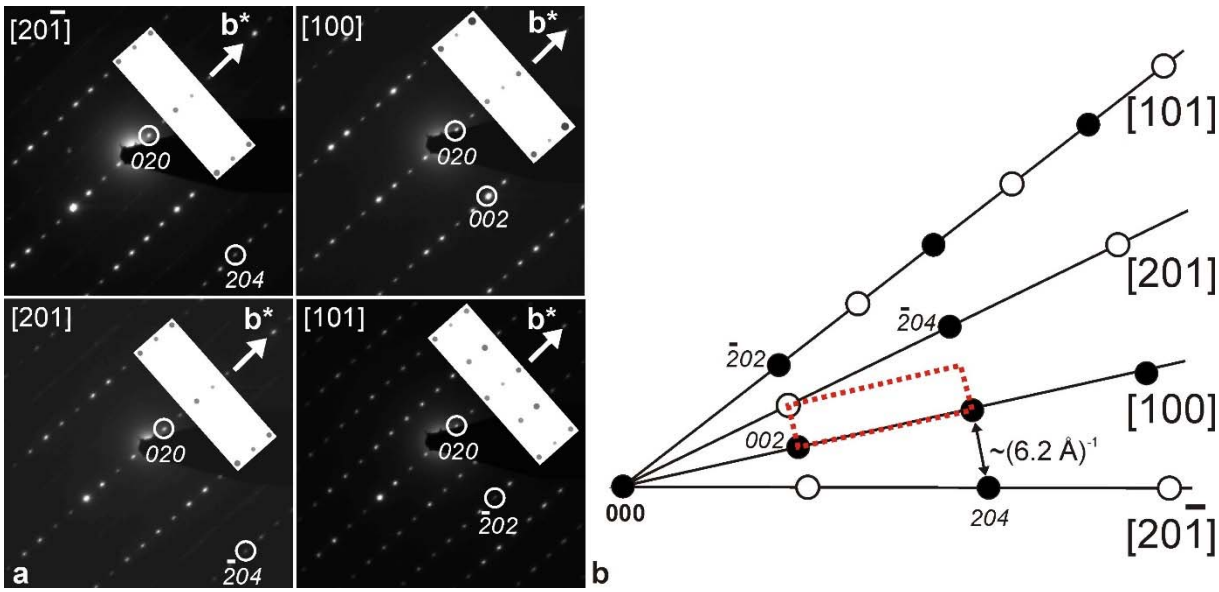

Figure 3.8: (a) SAED patterns of a $Bi_6S_2O_{15}$ fibre obtained from a tilt series with the rotation axis being the crystallographic **b*** axis. Some reflections are assigned with indices. Insets show sections of simulated SAED patterns with inverted contrast. (b) Reconstruction of the plane a^*b^*. Filled circles represent observed reflections and empty ones extinct reflections in the observed directions perpendicular to **b***. The extinctions indicate a doubling the third lattice parameter (2 x 6.2 Å) leading to the unit cell framed in red.

The observation of higher order Laue zones gives the distance between the lattice planes in direction of view and thus provides three-dimensional information. An alternative way for the full reconstruction of reciprocal space are tilting experiments: by recording SAED pattern of the same crystal in different directions and considering the angles between them, missing distances and lattice planes can be extrapolated. This is demonstrated here on the example of $Bi_6S_2O_{15}$ which crystallizes with a fibrous morphology.[19] The individual nanofibers are single

[18] T. Weber, J. Dshemuchadse, M. Kobas, M. Conrad, B. Harbrecht, W. Steurer. Large, larger, largest – a family of cluster-based tantalum copper aluminides with giant unit cells. I. Structure solution and refinement. *Acta Cryst. B***65** (2009) 308–317.

[19] Y. Zhou, J.-D. Grunwaldt, F. Krumeich, K. Zheng, G. Chen, J. Stoetzel, R. Frahm, G. R. Patzke. Hydrothermal Synthesis of $Bi_6S_2O_{15}$ Nanowires: Structural, in situ EXAFS, and Humidity-Sensing Studies. *Small* **6** (2010) 1173-1179.

crystalline and electron diffraction investigations were performed to determine the cell parameters. Two lattice parameters were retrieved from SAED patterns recorded in different orientations which further indicate the centering of a face and a glide plane. However, the determination of the plane perpendicular to the needle axis is a general problem during the characterization of such anisotropic structures. Therefore, a series of SAED patterns were obtained by rotating a fiber around an axis (here: **b***) and then reconstructing the reciprocal plane perpendicular to the rotation axis (Fig. 3.8). The d-values were determined with an accuracy of ca. ± 0.1 Å from the SAED patterns, the tilting angles between the patterns were measured with the goniometer of the TEM with an accuracy of ca. ± 1 degree. A distance of ca. 6.2 Å was found between the observed reflections but it must be doubled due to extinct reflections (Fig. 3.8b). The collected electron diffraction data obtained from the nanowires led to an orthorhombic unit cell with the approximate lattice parameters: $a \approx 12.4$ Å; $b \approx 19.8$ Å; $c \approx 5.8$ Å. The extinctions observed in the SAED patterns point to space groups with the partial symbol Cc--. This unit cell parameters are similar to those of the known bismuth chromate $Bi_6Cr_2O_{15}$ ($a \approx 12.30$ Å; $b \approx 19.875$ Å; $c \approx 5.882$ Å; SG *Ccc*2). The hypothesis that the two phases are isostructural could be verified by Rietveld refinement of the X-ray powder diffraction data ($a = 12.206(1)$ Å; $b = 19.611(2)$ Å; $c = 5.8388(7)$ Å; SG *Ccc*2) and simulations of the SAED patterns (Fig. 3.8a).

The discovery of the first quasicrystal by *D. Shechtman* represents an excellent example for a meticulous exploration of reciprocal space. When investigating a grain of AlMn alloy prepared by rapid cooling, he found a diffraction pattern exhibiting a unique tenfold symmetry that was not being allowed in classic crystallography. Besides that, he not only explored further diffraction patterns of this particle in other orientations but also measured the tilting angles between them. All results were in accordance with an icosahedral symmetry. These findings indeed provided a convincing proof for this new class of material (Nobel prize 2011).[20]

The quantitative evaluation of the reflection intensities as done in X-ray diffraction is impeded in electron diffraction by frequent multiple diffraction caused by strong electron-matter Coulomb interaction. This effect is strongest if the crystal is oriented along a zone axis as many lattice planes are in reflection condition. Multiple scattering can thus be minimized by tilting away from the zone axes. The use of precession methods accomplish this, and full 3D data sets for structure determination similar to single crystal X-ray diffraction are obtainable.[21]

3.1.4 Amplitude Contrast

Interactions that diminish the intensity of the direct beam, i.e. all scattering events, generate amplitude contrast as measured in the bright field (BF) mode that uses only the direct beam for image formation. In the TEM, a small objective aperture inserted into the back focal plane of the objective lens allows exclusively the direct beam to pass its central hole and to generate an image (Figs. 2.5 and 3.9a). Scattered and diffracted electrons are completely caught by the

[20] D. Shechtman, I. Blech, D. Gratias, J. W. Cahn. Metallic phase with long-range orientational order and no translational symmetry. *Phys. Rev. Lett.* **53** (1984) 1951-1954.
[21] E. Mugnaioli, T. Gorelik, U. Kolb. ‘‘Ab initio’’ structure solution from electron diffraction data obtained by a combination of automated diffraction tomography and precession technique. *Ultramicroscopy* **109** (2009) 758–765.

aperture. In a STEM, a bright field detector placed on the optic axis measures the intensity of the direct beam (Fig. 2.6).

The local reduction of the direct beam's intensity builds up the intensity distribution in BF images. A main component of this weakening is caused by the mass-thickness effect. The effect of large differences in mass between Au and Ti dominates the contrast in a BF-TEM image of gold particles on TiO_2 (Figure 3.9b). The particles with a size of several 10 nm appear black since Au is by far the heaviest element in this system and therefore scatters strongest which reduces the intensity of the beam there. Furthermore, the Au particles are crystalline and thus Bragg diffraction reduces the dark contrast further (see below). The TiO_2 support appears as almost uniformly grey material. However, the area in the upper right corner of the image is thicker than the centre and thus the contrast is darker there (thickness contrast).

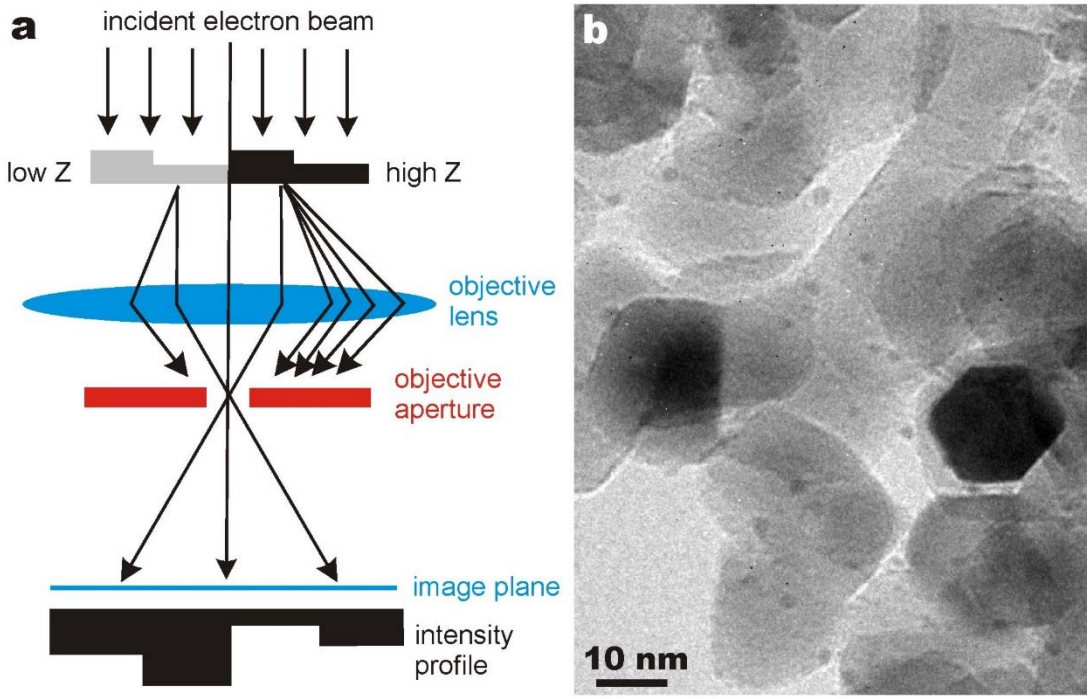

Figure 3.9: (a) Schematic representation of the contrast generation in BF-TEM. Only the direct beam passes through the central hole in the objective aperture and contributes to the final image whereas scattered and diffracted beams are blocked. (b) BF-TEM image of Au-NPs on TiO_2.

If a sample is crystalline, then another type of contrast appears in BF- and DF-TEM and STEM images, namely diffraction or Bragg contrast. If a crystal is oriented close to a zone axis, many electrons are strongly scattered to contribute to the intensities in the diffracted beams. Therefore, the intensity of such areas is reduced and they then appear dark in the BF image. On the other hand, such areas may appear bright in the DF-TEM image if they diffract into the area of reciprocal space that is selected by the objective aperture (see Fig. 2.5).

ZrO_2 microcrystals appear with different contrast in the BF-TEM image (Fig. 3.10a). Thickness contrast appears as the specimen is wedge-shaped and thin close to the hole at the bottom (bright) but thick at the top (dark). Of course, maximal brightness occurs in the hole of the specimen as all electrons pass there and contribute to the BF-TEM image. It is eye-catching that some ZrO_2 crystallites show up with higher darkness than those in their neighbourhood although the thickness is similar. These dark crystals are by chance oriented close to a zone axis

where much more electrons are diffracted than if they are in an arbitrary orientation. Therefore, the intensity of the direct beam that solely contributes to the image intensity distribution in the BF-TEM mode is reduced there, and such crystals appear relatively dark as a result. In the DF-TEM (Fig. 3.10b), a single diffracted beam is selected to pass through the objective aperture and to build up the image. Crystallites diffracting into that particular area of reciprocal space thus appear bright whereas others remain dark. Note that the hole in the specimen appears black as no scattering occurs there (Fig. 3.10b).

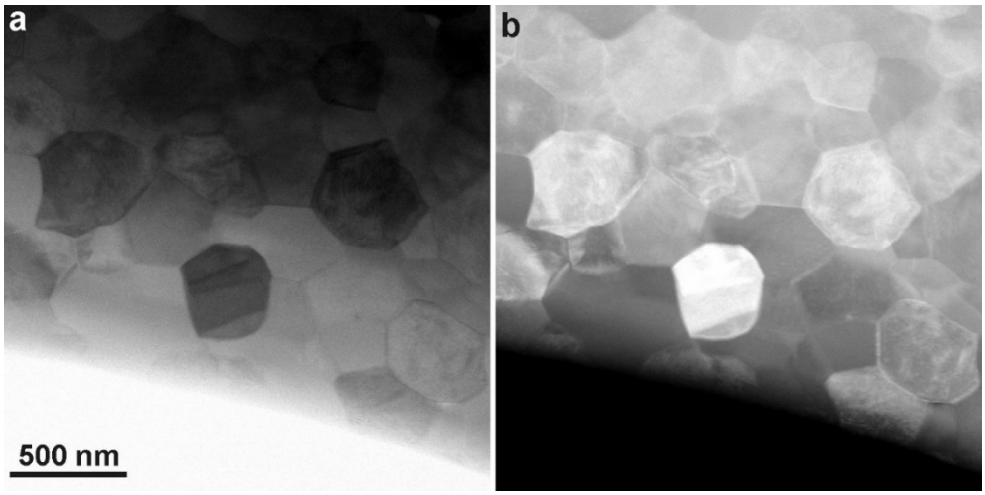

Figure 3.10: (a) BF-TEM and (b) DF-TEM image of ZrO_2 microcrystals.

The different mechanisms of contrast generation, namely mass-thickness and diffraction contrast, occur simultaneously in specimens that are at least partly crystalline. This renders the interpretation of BF- and DF-TEM and STEM images often complex and quite difficult in many cases.

3.1.5 Phase Contrast

Phase contrast images result from the interference of diffracted beams with each other and with the direct beam. Thus, to obtain lattice images, a large objective aperture has to be selected that permits many beams including the undiffracted one to pass (Fig. 2.5). If the point resolution of the microscope is sufficiently high and a suitable crystalline sample is oriented along a zone axis, then High Resolution Transmission Electron Microscopy (HRTEM) images are obtained. The diameter of the objective aperture is chosen in such way that reflections with frequencies k up to the point resolution of the microscope are collected.[22]

The incident parallel electron beam, considered as a plane wave, interacts ideally only elastically with the crystal potential while passing through the specimen. The resulting modulations of its phase and amplitude are then present in the electron wave leaving the specimen. This wave, the object exit wave $o(r)$, thus contains information about the object's structure. It is then interacting with the electron optic system of the microscope, most importantly the image forming objective lens. As all lenses, the objective lens is not ideal but

[22] Note that phase contrast can be achieved in STEM as well: F. Krumeich, E. Müller, R. A. Wepf. Phase-Contrast Imaging in Aberration-Corrected Scanning Transmission Electron Microscopy. *Micron* **49** (2013) 1-14.

suffers from aberrations, namely astigmatism, spherical (C_s) and chromatic (C_c) aberration. Their overall effect is the reduction of the image quality so that a point in the sample becomes a disk in the image. In thin samples (so-called weak-phase objects), the intensity distribution of the exit wave function is described by the phase contrast transfer function (PCTF) $sin(-\chi(k))$ which gives the phase shifts of diffracted beams with respect to the direct beam:

$$\chi(k) = \pi\lambda\Delta f k^2 + 1/2\pi C_s\lambda^3 k^4$$

This function $sin\chi(k)$ represents a complicated curve. It strongly depends on C_s (spherical aberration coefficient of the image-forming objective lens), on λ (electron wave-length as defined by the accelerating voltage), on the defocus, and on the spatial frequency k. While this function is zero at the origin, it becomes negative for intermediate values of k (Fig. 3.11). In this region of k, all information is transferred with negative phase contrast, i.e. atom positions appear dark in the HRTEM image. Therefore the intensity distribution in the image is directly interpretable under these conditions.

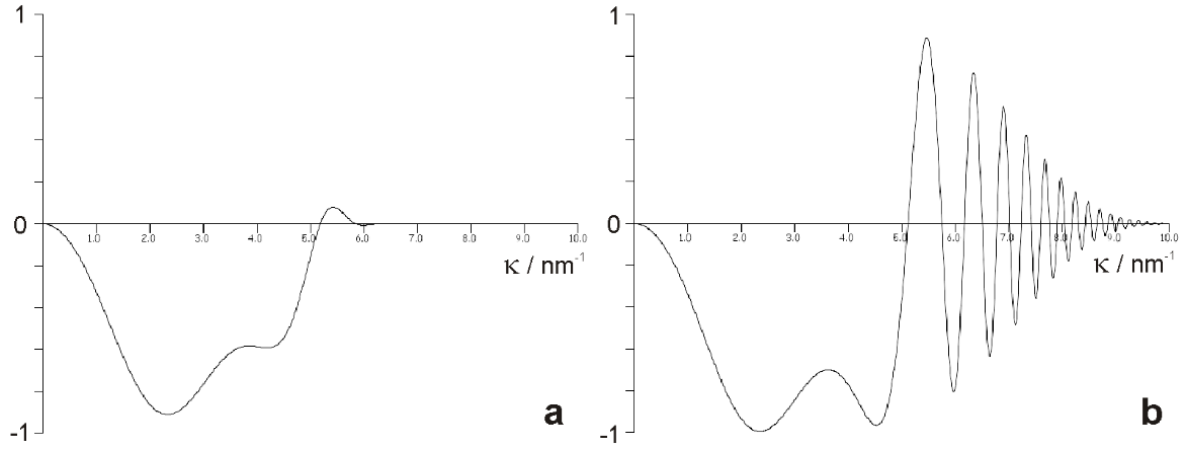

Figure 3.11: Phase contrast transfer functions PCTFs of two 300 kV TEMs close to Scherzer defocus (C_s = 1.15 mm, C_c = 1.5 mm). (a) LaB_6 cathode; PCTF crosses the κ axis at about 5.1 nm^{-1} which corresponds to a resolution of about 1.9 Å. (b) field-emission gun; in the more coherent electron beam of the FEG, the effect of damping is reduced compared to the LaB_6 cathode. As a result, there is additional information beyond the point resolution in the oscillating PCTF until the information limit at ca. 1.0 Å.

The point resolution of a TEM is defined as the first crossing of the PCTF with the k axis for the defocus when the area of negative information transfer is maximally extended towards high frequencies. This particular defocus is called Scherzer focus. Both the Scherzer focus Δf_s and the point resolution Δx are functions of C_s and λ:

$$\Delta f_s = -\sqrt{\frac{4}{3} C_s\lambda}$$

$$\Delta X = 0.66 \sqrt[4]{C_s\lambda^3}$$

Depending on the defocus, the PCTF oscillate strongly (Fig. 3.11). At larger k vectors, strong damping occurs which is mainly due to the effects of chromatic aberration, focus spread, and energy instabilities. Thus, the damping effect is strong for electrons coming from a LaB_6 cathode but much less for the more coherent electron beam produced by a FEG (Fig. 3.11).

Since the defocus is variable and can be adjusted at the microscope, an adequate value can be chosen to select optimized imaging conditions. As HRTEM images are formed by phase contrast, image simulations must be performed to understand their intensity pattern which depends not only on the crystal structure and the microscope's properties but also on the defocus and sample thickness.

The investigation of an amorphous carbon foil by TEM demonstrates the defocus dependence of the image contrast (Fig. 3.12). At Gaussian focus (defocus $\Delta f \approx 0$), there is a minimum of contrast so the rim of the foil is hardly visible. The Fourier transform of the image shows a bright disk of diffuse scattering. Defocussing the objective lens in both directions generates contrast (Fig. 3.12). In underfocus ($\Delta f < 0$), the rim of the carbon foil has a bright fringe whereas it is dark in overfocus ($\Delta f > 0$). The images recorded at $\Delta f \approx$ -80 nm and + 80 nm show both one black ring in their Fourier transforms while several rings appear at higher defocus values.[23] Such a ring indicates the complete lack of information transferred by the microscope at this particular defocus for this frequency κ. In fact, these black rings correspond to crossings of the PCTF with the κ axis. For example, an image was recorded at $\Delta f \approx$ -80 nm, which is close to Scherzer defocus, and thus the imaging conditions are similar to those described by the PCTF shown in Fig. 3.11a leading to a single dark ring.

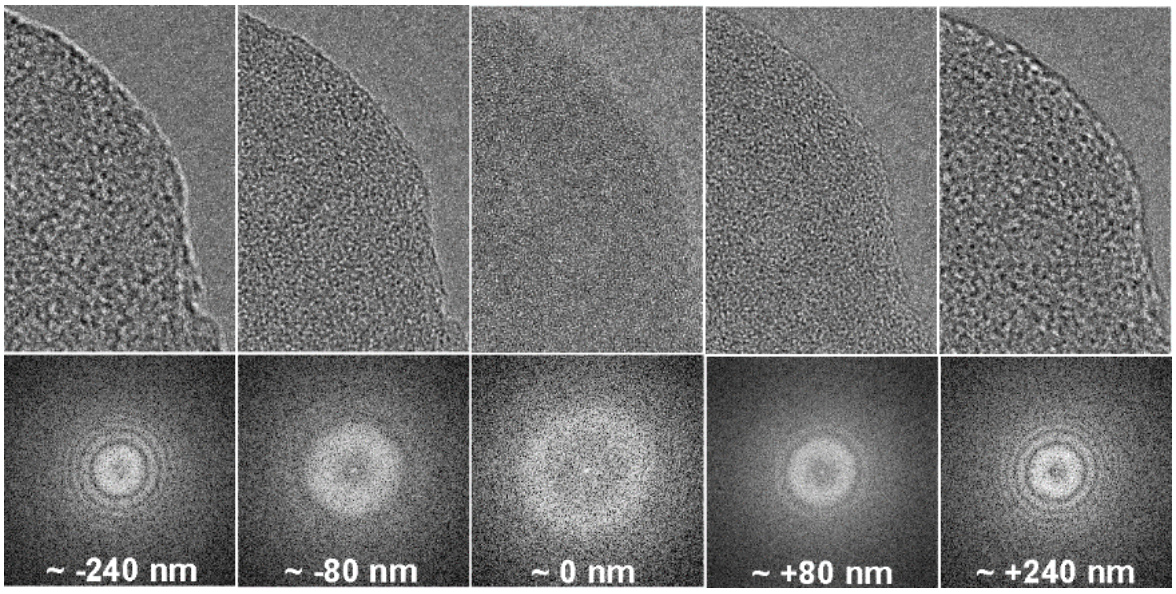

Figure 3.12: HRTEM images of amorphous carbon. Focus series with the approximate defocus value Δf given and the Fourier transform shown below the corresponding image.

Besides information about the defocus, the shape of the diffuse area in the center of Fourier transforms of images of amorphous regions helps to judge the quality of the imaging conditions: astigmatism leads to a deviation from the ideally circular shape and sample drift to distortions with extensions in one direction.

[23] The Fourier transforms shown here were calculated using the program *Digital Micrograph* (now: *Gatan Microscopy Suite* GMS3, http://www.gatan.com/products/tem-analysis/gatan-microscopy-suite-software). As an alternative, *ImageJ* is often used for image processing (https://imagej.nih.gov/ij/).

3.2 Inelastic Interactions

If energy is transferred from the incident electrons to the sample, then the energy of the electron after its inelastic interaction with the sample is reduced by a certain amount: $E_{el} < E_0$. The energy transferred to the specimen can cause different signals that depend on the material and are exploited by the various methods of analytical electron microscopy (AEM).

3.2.1 Overview

If a part of the energy that an incoming electron carries is transferred to the specimen, several processes can take part generating the following effects:

1. **Inner-shell ionisation**: The incident electron may transfer a part of its energy to an electron localized in an inner electron shell of an atom. Depending on the amount of energy transferred to this electron, it is either promoted into an empty electronic state or ejected into the vacuum. The resulting electronic state of this exited atom is energetically unstable as an inner shell with a low energy has an electron vacancy whereas levels of higher energy are occupied. This triggers an electron to drop down from a higher energy level and to fill the vacancy. The excess energy of the electron dropping to a lower state can be either emitted as a characteristic X-ray (see below) or neutralized by the generation of an Auger electron.
2. **Braking radiation** ("Bremsstrahlung"): The deceleration of electrons by the Coulomb force of the nucleus generates X-rays that can carry any amount of energy up to that of the incident beam: $E \leq E_0$.
3. **Secondary electrons** (SE): The work function of electrons located in the valence or conduction band is small and thus only the transfer of a small amount of energy is necessary to eject them into the vacuum. SEs have low energies (typically below 50 eV) and are utilized in SEM for observing morphology and surface topography.
4. **Phonons**: Phonons are collective oscillations of the atoms in a crystal lattice that can be initiated by the transfer of energy from an incoming electron. This amount of energy typically is small ($E << 1$ eV). Many such processes contribute to heating up the specimen, which may lead to beam damage. Note that phonon scattering leads to a deflection of the electron into high angles as measured by HAADF-STEM.
5. **Plasmons**: If the electron beam passes through an assembly of free electrons, like in the conduction band of metals, the up-take of energy (ca. 5-30 eV) can induce collective oscillations of the electrons, the plasmons.
6. **Cathodoluminescence**: Electron-hole pairs are generated by promoting an electron from the valence band into the conduction band. This excited state is energetically instable. It can relax by filling the hole in the valence band by the electron dropping down from the conduction band. This recombination process leads to the emission of a photon carrying the difference energy $\Delta E = h\upsilon$. The determination of the light wavelength is thus a way to measure the band gap in semiconductors.

3.2.2 X-Ray Spectroscopy

After the ionization of an atom leading to a vacancy in an inner electron shell, this electron hole may be filled up by an electron dropping down from a higher energy level (Fig. 3.13a).

The excess energy, which corresponds to the energy difference between the two energy levels, can be emitted as electromagnetic radiation in the form of an X-ray quantum. The energy difference between electronic states is typical for a certain element and thus the energies of the emitted X-rays (characteristic peaks) can be used for a qualitative analysis (Fig. 3.13b). In the X-ray spectrum, an uncharacteristic background is present caused by braking radiation. The intensities of the signals can be measured and be used for a quantitative analysis. Frequently, energy-dispersive X-ray spectrometers (EDXS) are used for recording X-ray spectra as they can easily be attached to any electron microscope. Furthermore, their parallel measuring mode quite quickly generates a spectrum covering the whole energy range. Wavelength dispersive spectrometers (WDS) provide a better energy resolution but with the drawback of long measuring times.

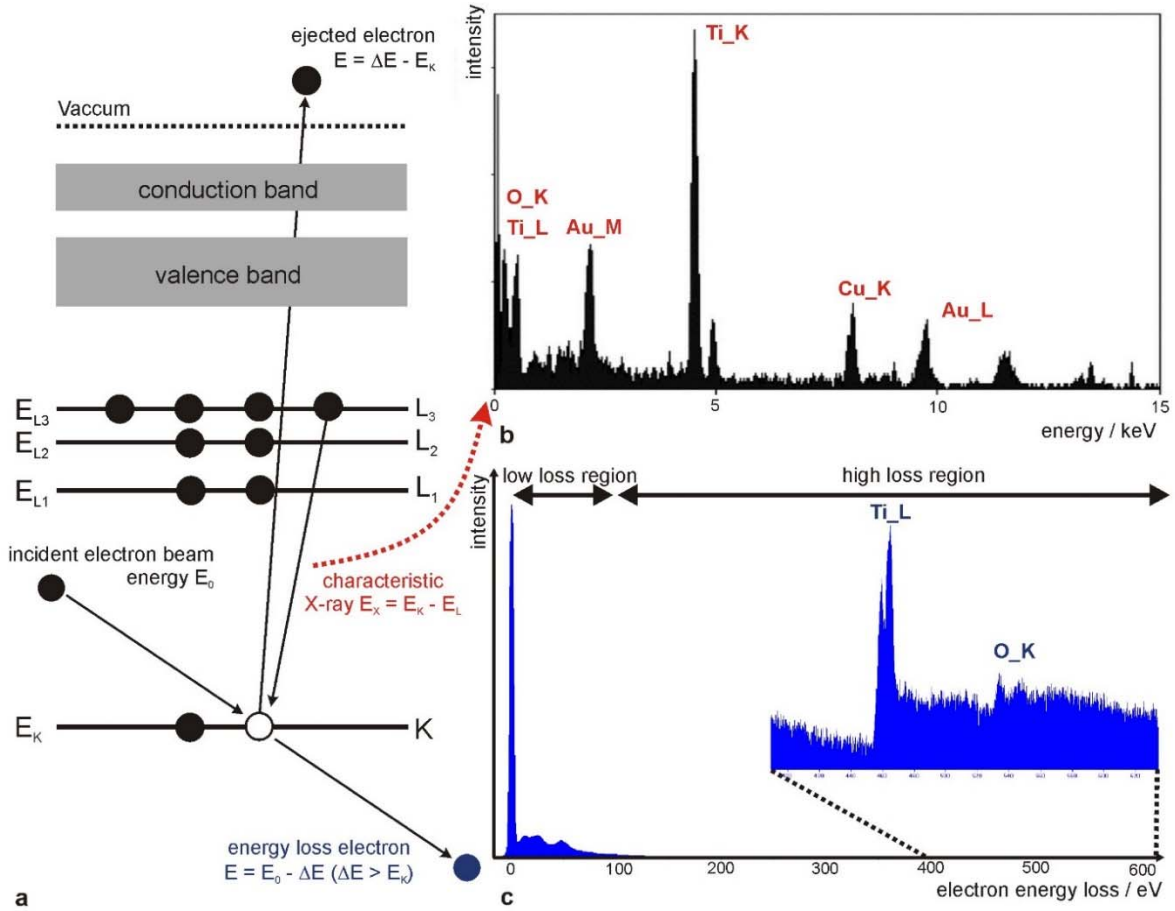

Figure 3.13: (a) Scheme of the generation of a characteristic X-ray. (b) Energy-dispersive X-ray spectrum (EDXS) of an Au/TiO_2 composite. Cu peaks arise from the TEM grid. (c) Electron energy loss spectrum (EELS) of TiO_2.

3.2.3 Electron Energy Loss Spectroscopy (EELS)

For the generation of the inelastic electron-matter interactions described above, energy is required that is transferred from an electron in the incoming beam. Consequently, this electron suffers a loss of energy that is measured by EELS. An EEL spectrum essentially comprises three different signals and energy ranges (Fig. 3.13c):[24]

1. **Zero loss (ZL) peak**: This peak contains all electrons that have passed the specimen

[24] R. F. Egerton. Electron energy-loss spectroscopy in the TEM. *Rep. Prog. Phys.* **72** (2009) 016502.

without any interaction at all or that have undergone an elastic interaction only. If the sample is thin, the ZL peak is by far the most intense signal.

2. **Low loss region**: This region covers the range between the ZL peak and an energy loss of about 100 eV. The plasmon peaks are the predominant features here. From the intensity of these peaks and their relation to that of the ZL peak, information about the sample thickness can be derived: intense plasmon peaks point to a thick sample area.

3. **Core loss region**: Starting at an energy loss of ca. 100 eV, the signal intensity drops rapidly. All processes involving unspecific energy losses, in particular the braking radiation, contribute to this continuous background. Similar to X-ray spectra, there are pronounced peaks at certain energy losses in the EELS as well. Since these ionization edges appear at energy losses that are typical for an element, a qualitative analysis of a material by EELS is feasible. The onset of such an ionization edge corresponds to the threshold energy that is necessary to promote an inner shell electron from its energetically favoured ground state to the lowest unoccupied energy level (lowest unoccupied molecular orbital (LUMO)). This energy is specific for a certain shell of a certain element. Above this threshold energy, all energy losses are possible since an electron transferred to the vacuum might carry any amount of surplus kinetic energy. If the material has a well-structured density of states (DOS) around the Fermi level, not all transitions are equally likely. This gives rise to a fine structure of the intensity distribution in the energy loss range close to the ionization edge that reflects the DOS. The evaluation of this electron energy loss near edge structure (ELNES) can provide important information. It be used to probe the oxidation state, e.g. of transition metals like iron and manganese.[25] Remarkably, valence mapping is feasible as demonstrated for the distribution $Ce^{3+/4+}$ in cerium oxide.[26] The fine structure farther away from the ionization edge moreover carries valuable information about coordination and inter-atomic distances (extended energy loss fine structure, EXELFS).

3.2.4 EDXS vs. EELS

EEL and X-ray spectroscopy are complimentary analytical methods in several aspects. Both utilize the ionization of atoms by an electron beam and the measured signals are useful for compositional analyses. EELS works best in an energy loss region below ca. 1000 eV because at even higher energy losses the intensity decreases drastically. In this region, the K edges of the light elements occur that are not or less efficiently detected by X-ray spectroscopy. The energy resolution in EELS (well below 1 eV) is much better than that in X-ray spectroscopy (~100 eV) and enables one to observe fine structures of the ionization edges. Peak overlap is a frequent problem in EDXS. The ionization edges of O_K and Ti_L, for instance, are well separated in EELS while they overlap in EDXS (Fig. 3.13b,c). The details observed in EEL spectra provide a lot of information so that this method profits most from the improved energy

[25] H. K. Schmid, W. Mader. Oxidation states of Mn and Fe in various compound oxide systems. *Micron* **37** (2006) 426–432.

[26] B. Goris, S. Turner, S. Bals, G. Van Tendeloo. Three-dimensional valency mapping in ceria nanocrystals. *ACS Nano* **8** (2014) 10878–10884.

resolution offered by a cold field emitter (ΔE ≈ 0.35 eV) or a monochromator (ΔE ≈ 0.15 eV) compared to a standard FEG (ΔE ≈ 0.5 – 1 eV).

3.2.5 Analytical Electron Microscopy (AEM)

The ultimate goal of analytical electron microscopy is to characterize the elemental composition at every site of a specimen with atomic resolution. Thus, performing laterally resolved EDXS and EELS spectroscopy to get information about the chemistry at a spot, along a line or in an area has become a main task in practical work. The maximum of obtainable information is represented by the so-called data cube: for each pixel in the STEM image, the full spectral information is available. Two approaches are used to get this data cube: (i) either a spectrum is recorded for every spot in an image (STEM-coupled EDXS and EELS) or (ii) energy-selective images of a selected area are recorded for many energies (energy-filtered TEM).[27]

(i) The highly localized signal from the specimen that is obtained in STEM can be exploited in AEM by the combination with spectroscopic methods. From this, information about the composition at any spot or area in the image is retrievable. This STEM spectrum imaging method is used to generate elemental maps that visualize the elemental distribution in selected specimen areas.

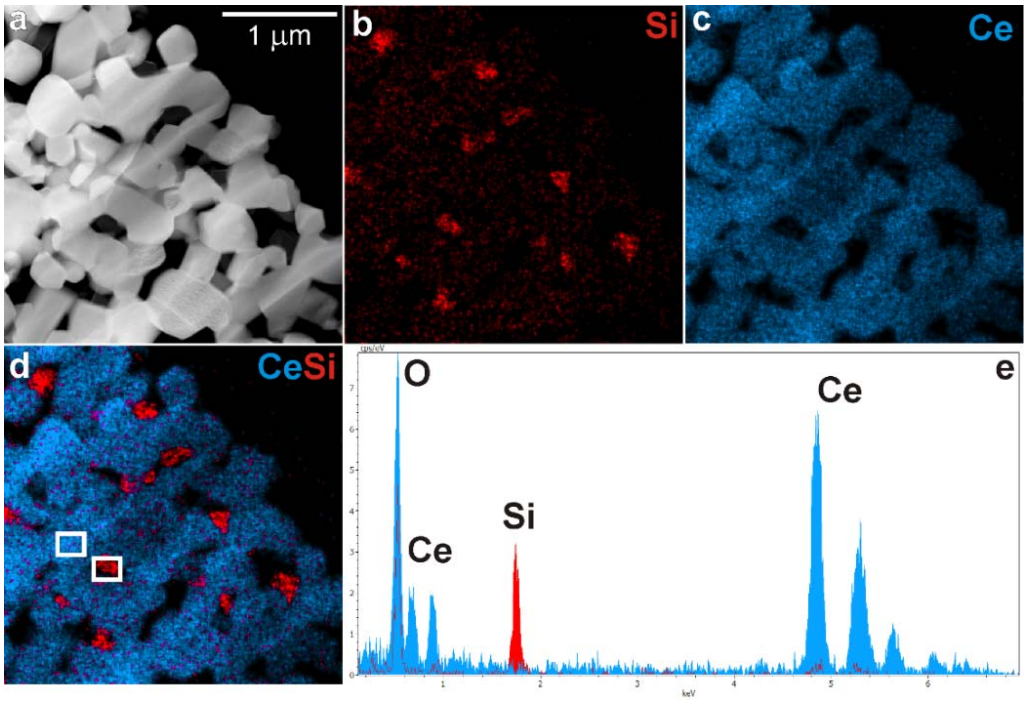

Figure 3.14: Mixture of zeolite and CeO_2 crystals: (a) HAADF-STEM image. EDXS mappings of (b) Si (K edge) and (c) Ce (L edge) and (d) composite map. (e) EDX spectra extracted for the two areas marked in (d).

In the HAADF-STEM image of a mixture of zeolite and CeO_2, the small zeolite crystals are dark and as the result hardly recognizable (Fig. 3.14a). The EDXS mappings of Si and Ce directly show the respective position of the oxides (Fig. 3.14b,c). The addition of the two

[27] W. Sigle. Analytical transmission electron microscopy. *Annu. Rev. Mater. Res.* **35** (2005) 239-314.

images leads to a SiCe composite map (Fig. 3.14d) that reveals the incorporation of the SiO_2-based zeolite crystals between the CeO_2 crystals. The production of coloured elemental distribution maps from the data cube (an EDX spectrum for each pixel in the image) renders this mapping technique very popular. However, the real scientific value is that now spectroscopic information for any spot, line or area in the image is extractable. The spectra obtained for the two areas marked in Fig. 3.14d confirm that the red coloured sites indeed are zeolite whereas the blue ones are CeO_2. This confirmation is essential for a reliable interpretation of the elemental maps – a fact that is often neglected in practise. Showing such qualitative elemental maps alone is dangerous and scientifically almost worthless as the presence of a colour just state that there is some intensity at a selected energy range.

(ii) The alternative method to STEM-coupled spectroscopy is energy-filtered TEM (EFTEM): an imaging filter is either mounted below the column of a TEM (post-column filter) or integrated in the microscope column (in-column filter). The filter is used to record images at a selected range of electron energy loss. The imaging filter consists of two main parts: the magnetic prism in which electrons with different energies are dispersed in a curved magnetic field and the optical column that either forms images with electrons of a selected energy range (energy-spectroscopic imaging, ESI) or records the EEL spectrum with a CCD camera. This method also fills the data cube, namely by recording images at subsequent energy ranges. Due to the selection of certain energy ranges, this technique has a reduced energy resolution compared to STEM-coupled EELS.

The so-called three-window method is mostly applied for elemental mappings using EFTEM (Fig. 3.15): an image is taken after a suitable ionisation edge of the corresponding element (post-edge image (ΔE_3)) and two additional images (pre-edge 1 (ΔE_1) and 2 (ΔE_2)) are recorded at energy losses smaller than the ionisation edge. Only the electrons passing through the selected energy slit contribute to these images. The pre-edge images are used for an approximate determination of the unspecific background that is then subtracted from the post-edge image leading to an elemental map with enhanced contrast. Alternatively, the intensity in the post-edge image and in a pre-edge image are divided pixel by pixel (so-called jump ratio method).[28]

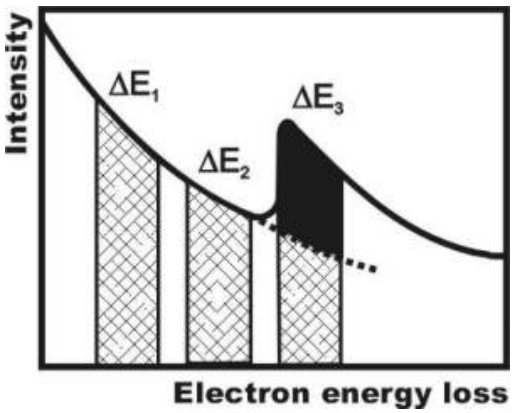

Figure 3.15: Scheme demonstrating the three-window technique.

Figures 3.16 and 3.17 show results obtained for a Ba-Ce oxide. The BF-TEM image shows an inhomogeneous sample with particles of different size (Fig. 3.17a). The Ce and Ba elemental maps were obtained at the respective M line with the three-window technique. The pre-edge and post edge images of Ba show all particles with a bright contrast with the intensity of the big

[28] F. Hofer, P. Warbichler, W. Grogger. Imaging of nanometer-sized precipitates in solids by electron spectroscopic imaging. *Ultramicroscopy* **59** (1995) 15-31.

crystals increased in the post-edge image. In fact, the Ba_M pre-edges image are post-edge images of oxygen (O_K line at 532 eV) so that all oxidic material appears bright. Nonetheless, the calculated Ba_M map shows that the big crystal indeed are BaO (Fig. 3.16). O the other hand, the energy of the Ba_M and Ce-M edge are rather close together (Fig. 3.17d). Therefore, the Ce pre-edge images are post-edge images of Ba so that the BaO crystals appear bright. In the Ce-M post-edge image, the brightness of the small particles is much increased compared to the pre-edge images (Fig. 3.16). The calculation of the Ce_M map by the three-window technique clearly takes this into account and consequently only the small particles appear bright.

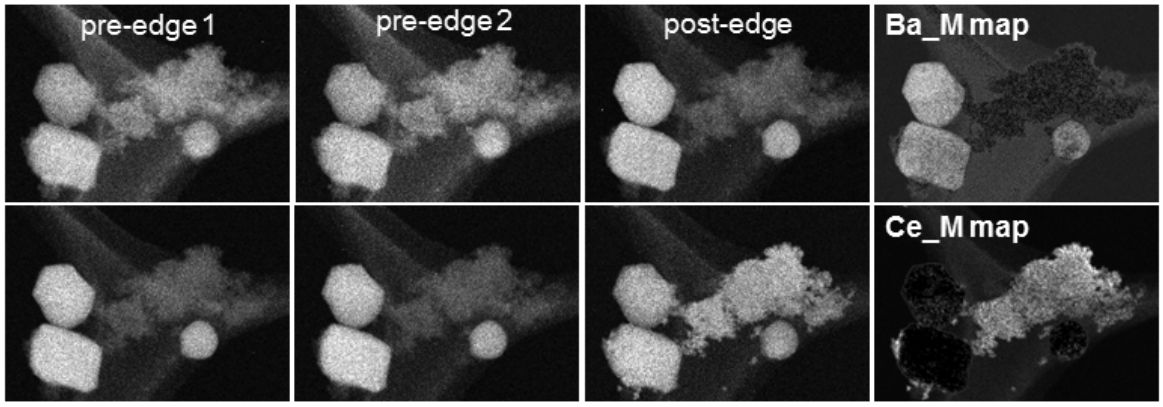

Figure 3.16: Mixed Ba-Ce oxide. Images used for the construction of the Ba (top row) and Ce (bottom row) elemental maps with the three-window technique.

The coloured elemental distribution map constructed by addition of the two individual elemental maps obtained by the three-window method reveals that the large crystals contain Ba while the smaller particles contain Ce (Fig. 17b). Sections of the EDX spectra of the two different areas (Fig. 3.17c) confirm the presence of Ba and Ce there as indicated by the presence of the corresponding M emission peaks. Note that a part of these peaks overlap, a common problem in EDXS that in some cases hinders an unambiguous identification of elements. The relevant part of the EELS is shown in Fig. 3.17d with the M ionization edges of the two elements. The M_4 and M_5 edges of Ba (781 and 796 eV) and Ce (883 and 901 eV) are prominent features and clearly separated. This example demonstrates that the energy resolution of EELS is superior to that of EDXS (*cf*. 3.2.4).

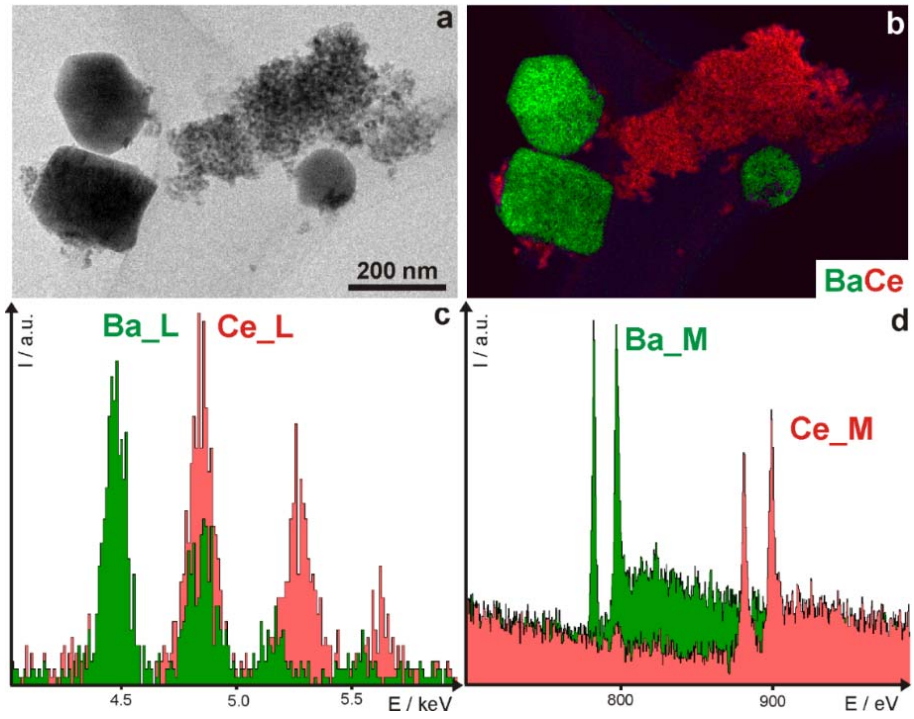

Figure 3.17: Mixed Ba-Ce oxide. (a) TEM image. (b) Elemental map by **e**nergy-**s**pectroscopic **i**maging (ESI) revealing the inhomogeneous distribution of Ba (green) and Ce (red). Sections of the (c) EDX and (d) EEL spectra of areas consisting of BaO and CeO_2, respectively.

4 SAMPLE PREPARATION

The strong interaction between the electron beam and any material requires that a TEM sample is thin enough so that electrons are able to pass through it. The actually advantageous specimen thickness depends on its material and on the technique applied for the investigation. Samples thinner than 10 nm give optimum results in HRTEM, while for other TEM investigations such as defect analyses they might be several 100 nm thick. In AEM, a large thickness is an advantage for EDXS to achieve a good signal:noise ratio whereas EELS requires thin areas.

4.1 Preparation of powders

In many cases such as microcrystalline samples, it is sufficient to grind the material in an agate mortar and to prepare a suspension of the powder in an inert solvent, mostly an alkane or an alcohol. Some droplets are then deposited on a thin carbon film that is supported by the bars of a metal grid (Fig. 4.1). After drying, the grid is mounted on the TEM holder. Nanoparticles, which are intrinsically thin, are often directly deposited on a TEM grid.

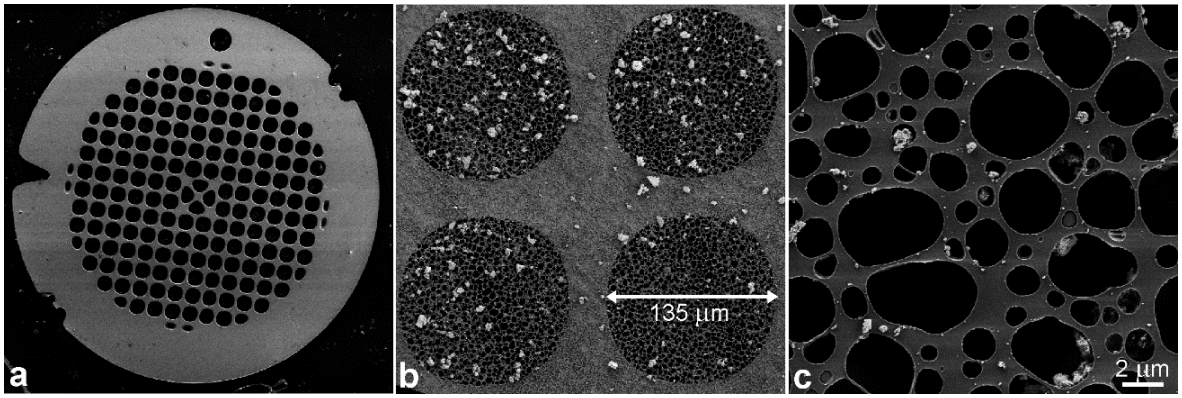

Figure 4.1: SEM images of (a) a TEM grid with a diameter of 3 mm, (b) four meshes of the grid supporting a holey carbon foil that carries a powdered sample and (c) details of (b).

For many applications such as HRTEM and EELS, it is an advantage to use a holey carbon foil (Fig. 4.1b,c): then some particles or crystals are at least partly extended into the hole so that these areas can be investigated without having a disturbing background of amorphous carbon. Fig. 4.2 shows an example: zeolite crystals are distributed on a holey carbon foil with some crystals in the vacuum. The crystal structure is better visible there as on the carbon foil. This is particularly important when looking at amorphous material that has a similar appearance as the carbon foil (Fig. 4.2b): compare the image of the amorphous particle at the bottom with that of the carbon foil (upper right side).

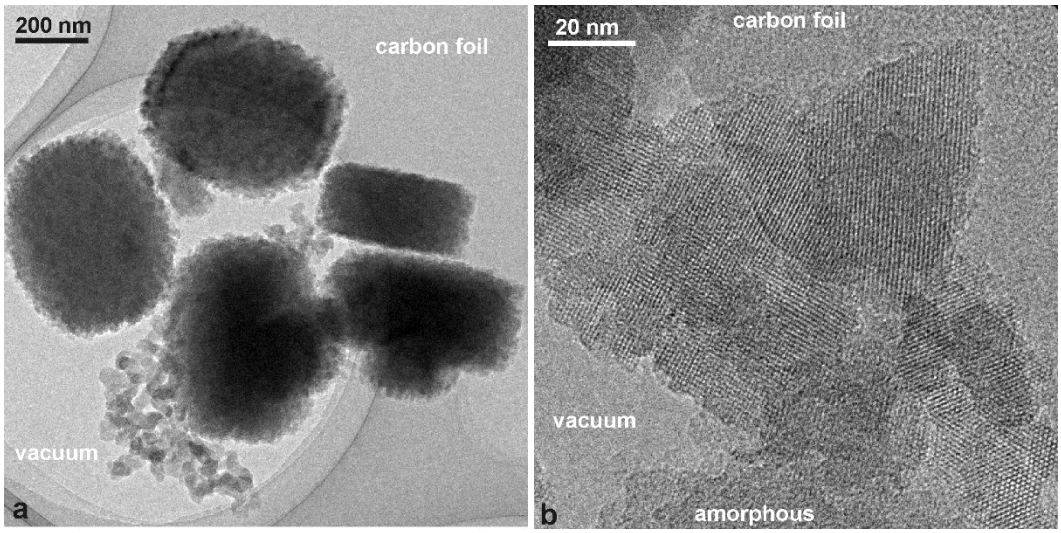

Figure 4.2: TEM images of zeolite crystals on a holey carbon foil. (a) Overview. (b) Detail with zeolite crystals partly being supported by the carbon foil and partly extending into a hole (vacuum). Some amorphous parts of the zeolite appear similar as the carbon foil.

4.2 Thinning of bulk samples

Compact samples must be prepared in such a way that the area of interest is transparent for electrons. Furthermore, the whole specimen must fit into the TEM holder that mostly requires disks of 3 mm in diameter. Various methods such as mechanical grinding, ion milling, chemical etching, electropolishing and combinations thereof are applied for specific bulk materials. These abrasive thinning methods might affect the structure and chemistry of the sample so that the danger of generating artefacts exists and the interpretation of the experimental results has to be done with care.

A frequently used and very flexible strategy is that of the cross-sectional preparation. This is useful to investigate layered structure formed on a support, for example a wafer. Here, two of the wafers are glued together forming a sandwich (Fig. 4.3). The sandwich is then embedded in a Cu pipe with an outer diameter of 3 mm. Thus, the final specimen fits into most TEM holders. Disks are then cut and thinned mechanically. The final ion milling step generates a hole in the centre of the specimen. Adjacent to the hole, wedge-shaped areas are present that are transparent for electrons. The advantage of this procedure is that any type of powder or nanomaterial can be embedded between the wafers (Fig. 4.3). In particular, anisotropic materials with a tubular or plate-like morphology can be prepared and investigated perpendicular to the extended direction.[29] Nanotubes, for example, lie flat on the wafer. When the formed sandwich is cut, then there is as good chance that the looked-for cross-sections of the nanotubes are indeed visible.

[29] E. Müller, F. Krumeich. A simple and fast preparation method for the TEM investigation of plate-like, needle-shaped and tubular materials in direction of the extensive axis. *Ultramicroscopy* **84** (2000) 143-147.

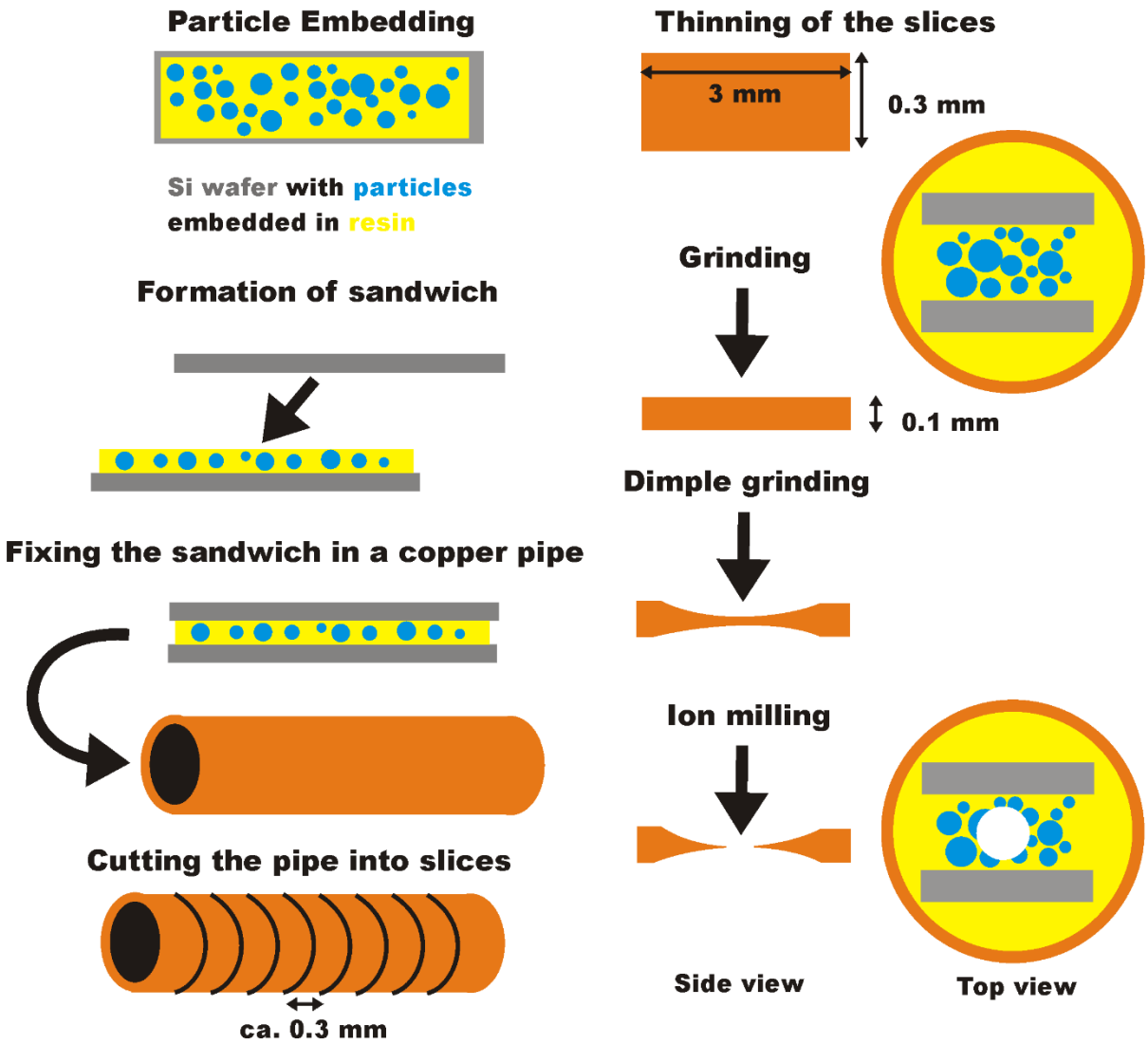

Figure 4.3: Scheme of the preparation for cross-sections and anisotropic materials. The first steps involve the embedding of the material, sandwich formation and its fixation in a copper pipe with resin (left side). Disks are cut from this pipe with a diamond wire saw. Then, the disks are abraded on both sides and then dimples are ground. Finally, a hole in the thin center of the disk is generated by an ion beam treatment (right side).

A rather recent development is the focussed ion beam (FIB) instrument that performs the abrasion of material by irradiation with a Ga ion beam (Fig. 4.4). It is now a versatile and widely applied method for preparation sample in various fields.[30] The strength of FIB as preparation tool is that the sample can be observed like in a standard scanning electron microscope and the area for preparing the TEM specimen can be selected with high local precision.

[30] (a) L.A. Giannuzzia, F.A. Stevie. A review of focused ion beam milling techniques for TEM specimen preparation. *Micron* **30** (1999) 197–204. (b) J. Mayer, L. A. Giannuzzi, T. Kamino, J. Michael. TEM sample preparation and FIB-induced damage. *MRS Bulletin* **32** (2007) 400-407.

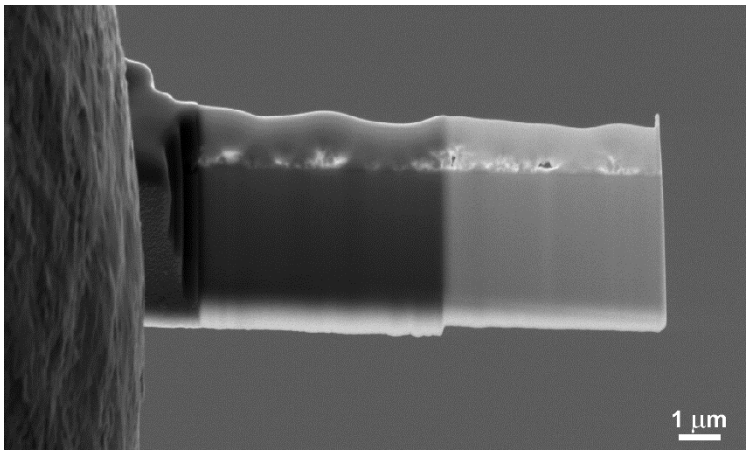

Figure 4.4: SEM image of a TEM lamella prepared by FIB.

4.3 Cleanliness of samples

Considering that with the aberration-corrected microscopes perfect imaging tools are available today, the preparation of a perfect and clean sample has become increasingly important for getting interpretable results, in particular when approaching the resolution limits. The most common problem is the contamination of the sample by a steadily growing carbon layer during the electron microscopy investigation. This is especially important for STEM studies. This deposition of a carbon layer on the specimen surface stems from the cracking of organic molecules. Those are attached to the surface of any TEM specimen or present even in the high vacuum of the microscope. The sample can be purified by treating it in a vacuum chamber with a plasma. An alternative way to reduce contamination inside the microscope, a procedure called "beam shower", is the irradiation of a large area of interest with an intense electron beam for several minutes.[31]

[31] D.R.G. Mitchell. Contamination mitigation strategies for scanning transmission electron microscopy. *Micron* **73** (2015) 36–46.

5 APPLICATIONS AND CASE STUDIES

5.1 HRTEM Study of Niobium Tungsten Oxides

Many transition metal oxides crystallize in quasi two-dimensional structures consisting of polyhedra that are stacked upon each other linked by corner-sharing along a short crystallographic axis. The projection of such structures can readily be imaged by HRTEM. An example is $Nb_8W_9O_{47}$ that crystallizes with a threefold superstructure of the tetragonal tungsten bronze (TTB) type (space group $P2_12_12$ with $a \approx 1.22$, $b \approx 3.66$, $c \approx 0.39$ nm).[32] The basic TTB unit consists of four five-rings of MO_6 octahedra (M = Nb,W) arranged around a central square. The threefold superstructure arises from the systematic occupation of 1/3 of the pentagonal channels with metal-oxygen strings resulting in a pentagonal bipyramid MO_7 (yellow in Fig. 5.1a). The bipyramid shares its equatorial edges with the surrounding five octahedra form a unit called pentagonal columns (PCs).[33] Such structures were high interest around 1970, and the structure of $Nb_8W_9O_{47}$ was one of the first that had been characterized by HRTEM visualizing all metal positions in projection.[34] Close to Scherzer defocus, the positions of all metals, which are by far the strongest scattering atoms here and thus have the highest contribution to the imaged projected crystal potential, are observed as dark patches in the HRTEM image (Fig. 5.1b). Image simulations have to be calculated taking into account the microscope and the crystallographic parameters to confirm that this direct interpretation of the HRTEM image is valid. Indeed, the experimental and the simulated image (JEMS program;[35] microscope: CM30 with U = 300 kV and C_s = 1.2 mm, crystal thickness = 3.9 nm and defocus = 30 nm)) match well (inset in Fig. 5.1b).

Fig. 5.1c shows a large area of a $Nb_8W_9O_{47}$ crystal which seems to be perfectly ordered on the first view. However, the arrangement of occupied pentagonal columns is not perfect. The PCs are arranged in pairs connected via a square of octahedra. Two such PC pairs occur in different orientations (blue and red in Fig. 5.1c). When studying their arrangement, the presence of a grain boundary between two perfectly ordered areas becomes apparent. In the boundary, the occupation of pentagonal tunnels and consequently the unit cells of the superstructure shifts by [1 1/3 0]. Remarkably, this defect concerns only the tunnel occupation but does not affect the basic TTB substructure (Fig. 5.1d). In the boundary, a PC pair is shifted in such a way, that a four-membered chain of PCs arises (yellow in Fig. 5.1d). This generates isolated PCs (orange) that are residuals of the other PC pairs.

---

[32] (a) A. W. Sleight. The crystal structure of $Nb_{16}W_{18}O_{94}$, a member of a $(MeO)_xMeO_3$ family of compounds. *Acta Chem. Scand.* **20** (1966) 1102-1112. (b) F. Krumeich, M. Wörle, A. Hussain Superstructure and Twinning in the Tetragonal Tungsten Bronze-Type Compound $Nb_7W_{10}O_{47}$. *J. Solid State Chem.* **149** (2000) 428-433.

[33] M. Lundberg, M. Sundberg, A. Magnéli. The `pentagonal column` as a building unit in crystal and defect structures of some groups of transition metal compounds. *J. Solid State Chem.* **44** (1982) 32-40

[34] S. Iijima, J. G. Allpress. Structural studies by high-resolution electron microscopy: tetragonal tungsten bronze-type structures in the system Nb_2O_5-WO_3. *Acta Crystallogr. A* **30** (1974) 22-29.

[35] P. A. Stadelmann. EMS - a software package for electron diffraction analysis and HREM image simulation in materials science. *Ultramicroscopy* **21** (1987) 131-145. http://www.jems-saas.ch/

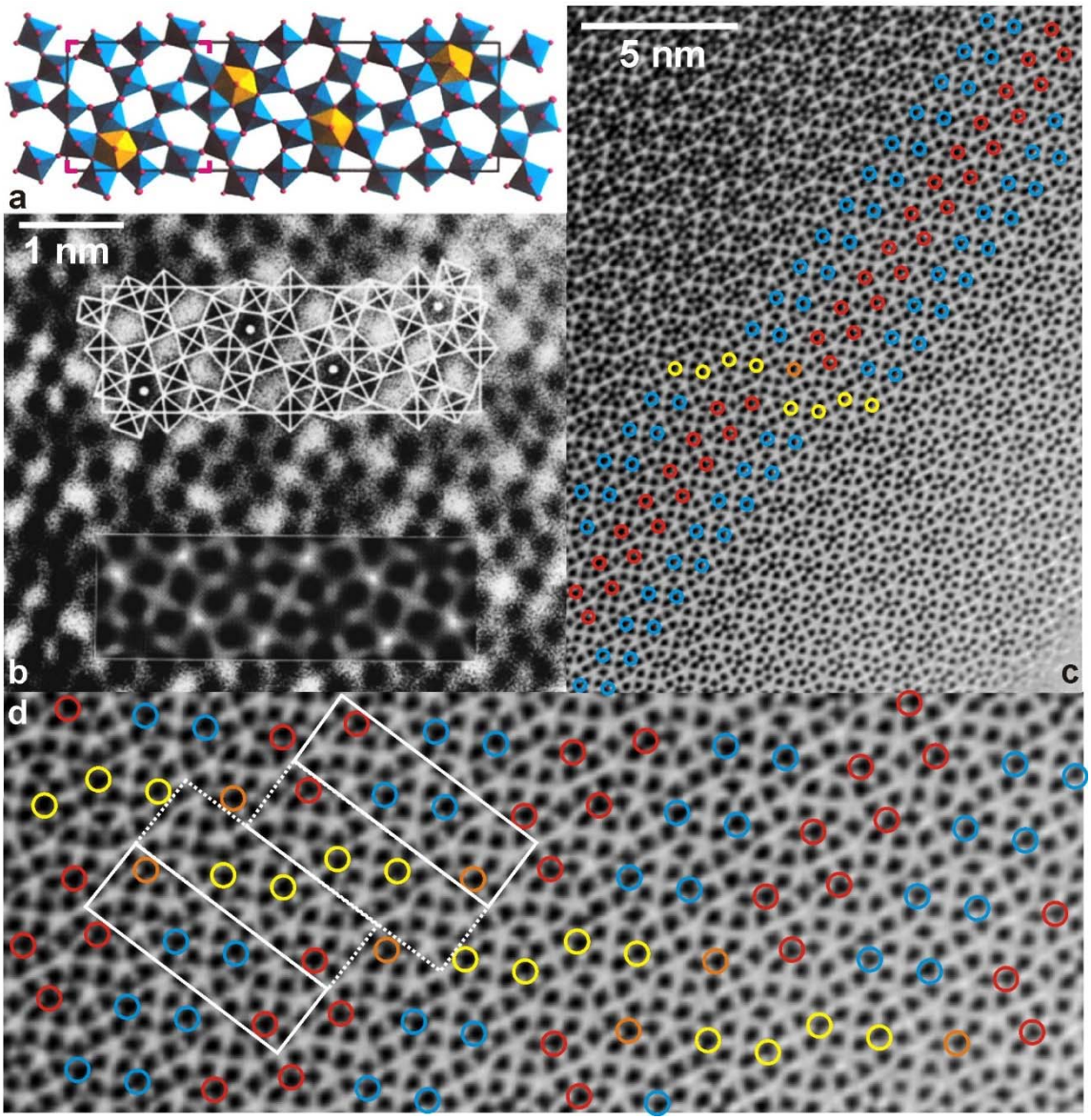

Figure 5.1: $Nb_8W_9O_{47}$ in projection along [001]. (a) Representation of the threefold superstructure of the tetragonal tungsten bronze type (TTB). A TTB subcell is marked. (b) HRTEM image with the structure representation and a simulation fitted in. (c) HRTEM image of a large area showing a grain boundary. (d) Magnification of (c). The shift of the unit cells (framed) is due to irregularly occupied pentagonal channels (encirled).

Besides the fully oxidized $Nb_8W_9O_{47}$, a series of mixed oxides $(Nb,W)_{17}O_{47}$ exists in which Nb^{5+} is substituted by in equal amounts by W^{6+} and M^{4+} maintain the metal:oxygen ratio but changing the ratio Nb:W.[36] The oxidation of these phases at different temperatures creates interesting new structural features.[37] The high-temperature oxidation product of $Nb_4W_{13}O_{47}$ represents an intergrowth of the TTB-type structure and segregations of WO_3. As in the case of $Nb_8W_9O_{47}$, all metal position are represented by dark dots in the HRTEM image recorded along

[36] F. Krumeich, A. Hussain, C. Bartsch, R. Gruehn. Zur Präparation und Struktur gemischtvalenter Niob-Wolframoxide der Zusammensetzung $(Nb,W)_{17}O_{47}$. *Z. anorg. allg. Chem.* **621** (1995) 799-806.

[37] (a) F. Krumeich. Oxidation products of $Nb_7W_{10}O_{47}$: a transmission electron microscopy study. *J. Solid State Chem.* **119** (1995) 420-427 (b) F. Krumeich, C. Bartsch, R. Gruehn. Oxidation products of $Nb_4W_{13}O_{47}$: a transmission electron microscopy study. *J. Solid State Chem.* **120** (1995) 268-274.

the short crystallographic axis (Fig. 5.2a). WO_3 crystallizes in a slightly distorted ReO_3-type structure and thus such segregations are recognizable in the image as a square array of dark spots. In analogy to the interpretation of the HRTEM image of $Nb_8W_9O_{47}$, all dark patched in the TTB-type structure can be assigned to either an MO_6 octahedron or an MO_7 pentagonal bipyramid. Thereby, a structural model for the defect structure can be derived from the HRTEM image. Remarkably, the HAADF-STEM image of a similar area (Fig. 5.2b) provides even more information: besides the positions of the metal atoms imaged now as bright spots, their brightness depends on the ratio W:Nb of the respective atomic column (Z contrast). As W has a higher Z than Nb ($Z_W = 74 > Z_{Nb} = 41$), W-rich atom positions appear brighter than Nb-rich ones (intensity increases with $\sim Z^2$).[38]

In addition to visualizing the metal positions by standard TEM and STEM, equatorial oxygen positions are recognizable in the phase and modulus of the specimen's exit plane wave obtained by focus series reconstruction.[39] Consequently, this method provides valuable supplementary information about distortions of the MO_6 octahedra in bronze-type oxides.

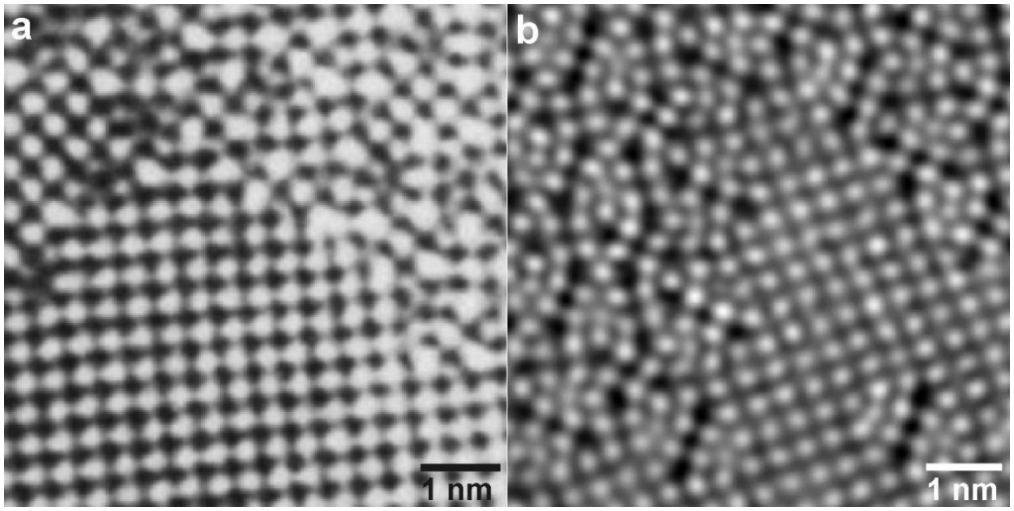

Figure 5.2: (a) HRTEM and (b) HAADF-STEM images of an oxidation product of $Nb_4W_{13}O_{47}$.

5.2 Order and Disorder

HRTEM is a powerful method not only for imaging perfect structures but also and even more importantly for detecting and characterizing defects and less-ordered structures. An example has already been discussed in the previous chapter with the dislocation of the occupied channels in an otherwise perfectly ordered TTB-type structure (cf. Fig. 5.1c). Some typical examples for different types and different degrees of disorder will be presented and discussed in the following.

[38] (a) A. I. Kirkland, W. O. Saxton. Cation segregation in $Nb_{16}W_{18}O_{94}$ using high angle annular dark field scanning transmission electron microscopy and image processing. *J. Microscopy* **206** (2002) 1-6. (b) F. Krumeich, R. Nesper. Oxidation products of the niobium tungsten oxide $Nb_4W_{13}O_{47}$: a high-resolution scanning transmission electron microscopy study. *J. Solid State Chem.* **179** (2006) 1857-1863.

[39] (a) A. I. Kirkland, R. R. Meyer. "Indirect" high-resolution transmission electron microscopy: aberration measurement and wavefunction reconstruction. *Microsc. Microanal.* **10** (2004) 401–413. (b) A.I. Kirkland, J. Sloan, S. Haigh. Ultrahigh resolution imaging of local structural distortions in intergrowth tungsten bronzes. Ultramicroscopy **107** (2007) 501–506.

5.2.1 Planar Defects

Many structure types are structurally very flexibe and allow the addition or removal of whole layers creating planar defects. The ReO_3 type is the parent structure for several derivatives. The structure solely comprises ReO_6 octahedra that are linked by corner-sharing along the three axes of a primitive cubic lattice. Perhaps the best-known variants of this structure are reduced WO_{3-x} phases that accommodate the loss of oxygen by introducing edge-sharing by the so-called crystallographic shear operation.[40] In the block structures, the introduction of edge-sharing between octahedra occurs in two orthogonal planes. The number of corner-sharing octahedra between the two shear-planes defines such a [NxM] block which in fact correspond to cuttings of the ReO_3 structure. Perpendicular to this plane, all octahedra are connected via corner-sharing so that the important structural features are recognizable in HRTEM images recorded along this direction.

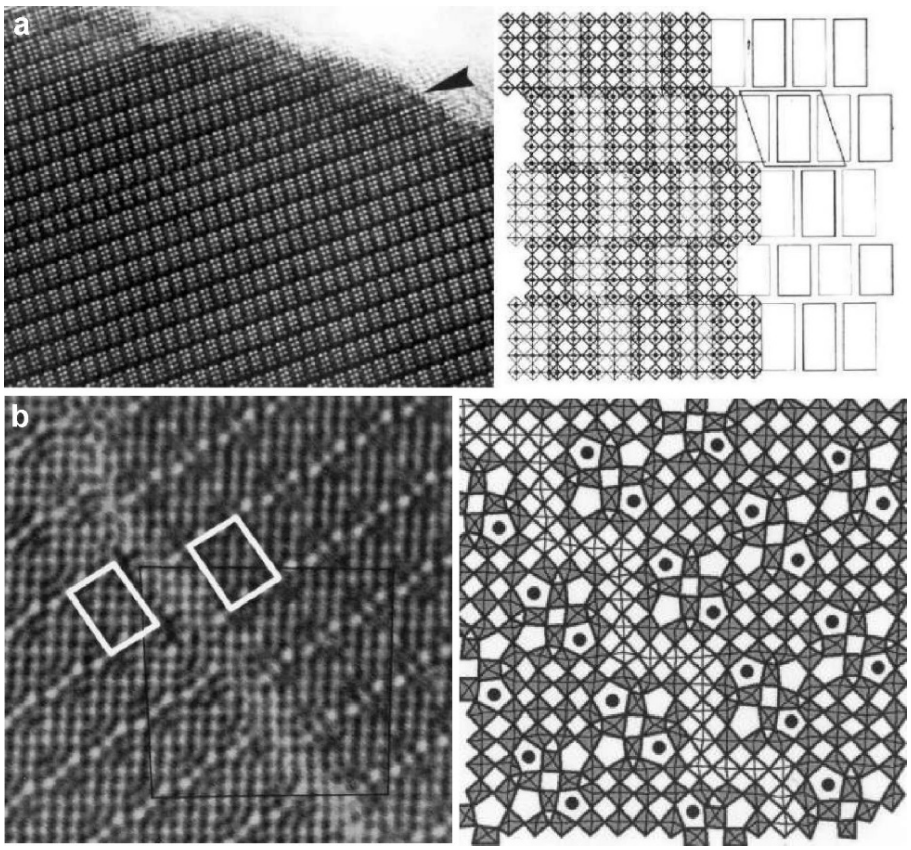

Figure 5.3: Examples of planar defects. HRTEM image of $ZnNb_{14}O_{35}F_2$ (a) and of $Zr_xNb_{8-2x}W_{12+x}O_{56}$ (b). Structural models are shown on the right. Most part of this areas are perfectly ordered but layers consisting of [3x4] blocks (a) and of additional octahedra (b), respectively, are coherently incorporated into the matrix structure.

Many niobium oxides and Nb_2O_5-rich phases crystallize in block structures. An example is the structure of $ZnNb_{14}O_{35}F_2$ (Fig. 5.3a) that consists of 3x5 corner-sharing octahedra ([3x5] blocks).[41] The sites of the shear planes appear dark in the images recorded with a TEM with

[40] A. Magnéli. Tungsten oxides from Scheele to our times – law of constant proportions versus non-stoichiometry and structural disorder. *Chem. Scripta* **26** (1986) 535-546.

[41] F. Krumeich, R. Gruehn. Präparation und durchstrahlungselektronenmikroskopische Untersuchung von $ZnNb_{14}O_{35}F_2$. *Z. anorg. allg Chem*. 570 (1989) 133-137.

limited resolution (ca. 3.5 Å). The distances between the metal atoms in these planes is rather small which leads to high scattering potential there. The square channels in the structure appear as bright dots. Thus, a [3x5] block appears in the HRTEM image as an array of 2x4 bright dots. Such structures easily allow the coherent incorporation of a plane consisting of blocks with different size. Here the planar defect consists of [3x4] blocks instead of the regular [3x5] blocks (Fig. 5.3a).

A new intergrowth structure between WO_3 and TTB type was found in a Zr-doped Nb-W oxide.[42] The metal positions appear in the HRTEM image as black dots. This knowledge allows the direct derivation of a structural model for the observed area (cf. Fig. 5.1b). The planar defect observed here consists of an additional plane of corner-sharing octahedra (Fig. 5.3b).

5.2.2 Intergrowth

Many phases that crystallize in closely related structures derived by crystallographic shear from the ReO_3 type form defects caused by intergrowth of them. A new type was found in the system Al-W-O.[43] In this structure, slabs of corner-sharing WO_6 octahedra (cuttings from the ReO_3-type WO_3 structure) are connected via Al-containing planes (Fig. 5.4a). The positions of the octrahedra on both sides of these planes are shifted in respect to each other so that a centered unit cell results. Strong reflections in the electron diffraction patterns correspond to the ReO_3 substructure (Fig. 5.4b,e). Additional weak reflections present along one axis between the main reflections (Fig. 5.4b) point to an ordered fourfold superstructure. In addition, the absence of every second reflection points to a centering of the unit cell in the observed plane. Due to the centering, the superstructure is in fact eightfold. The HRTEM image of a crystal with a tenfold superstructure (Fig. 5.4c) shows a perfectly ordered area with ReO_3-type slabs that are five octahedra wide. The proposed tetragonal structural model for $Al_4W_{10}O_{32}$ (a = 3.75, c = 39.5 Å; SG $I4/mmm$) consists of slabs of [5 x ∞ x ∞] corner-sharing WO_6 octahedra that are connected via edge-sharing to AlO_6 octahedra (Fig. 5.4a).

Several well-ordered crystals areas were found with similar phases with the only difference being the varying width of the slabs as defined by number of octahedra. The flexible structural principle and the close structural relationship between these phases allows intergrowth. An example is shown in Fig. 5.4d where slabs with width of four and six octahedra are incorporated coherently into the main structure with the tenfold superstructure having five octahedra wide slabs. The electron diffraction pattern of a highly disordered area does not show any well-defined superstructure reflections but diffuse streaking between the basic ReO_3-type reflections (Fig. 5.4e). For these Al-W oxides, all transitions from sharp superstructure reflections, indicating well-ordered phases, to diffuse streaks, indicating disorder, occur in the electron diffraction patterns of different crystallites. HRTEM images confirm these findings directly. Besides well-ordered areas (Fig. 5.4c,d), highly disordered areas were found. Fig. 5.4e shows an intergrowth of mainly the tenfold and the twelvefold superstructure. Another area contains

[42] F. Krumeich, G. Lietke, W. Mader. A novel intergrowth structure between ReO_3-Type and tetragonal tungsten bonze-type in the Zr/Nb/W/O system. *Acta Crystallogr. B* **52** (1996) 917-921.

[43] F. Krumeich, G. R. Patzke. A series of aluminum tungsten oxides crystallizing in a new ReO_3-related structure type. *J. Solid State Chem.* **181** (2008) 2646-2652.

many different slab widths including the broadest slab observed yet which is nine octahedra wide (Fig. 5.4f).

This study exemplifies the impressive power of the combination of electron diffraction and lattice imaging to uncover all the structural details of such a complex and defective mixture of phases.

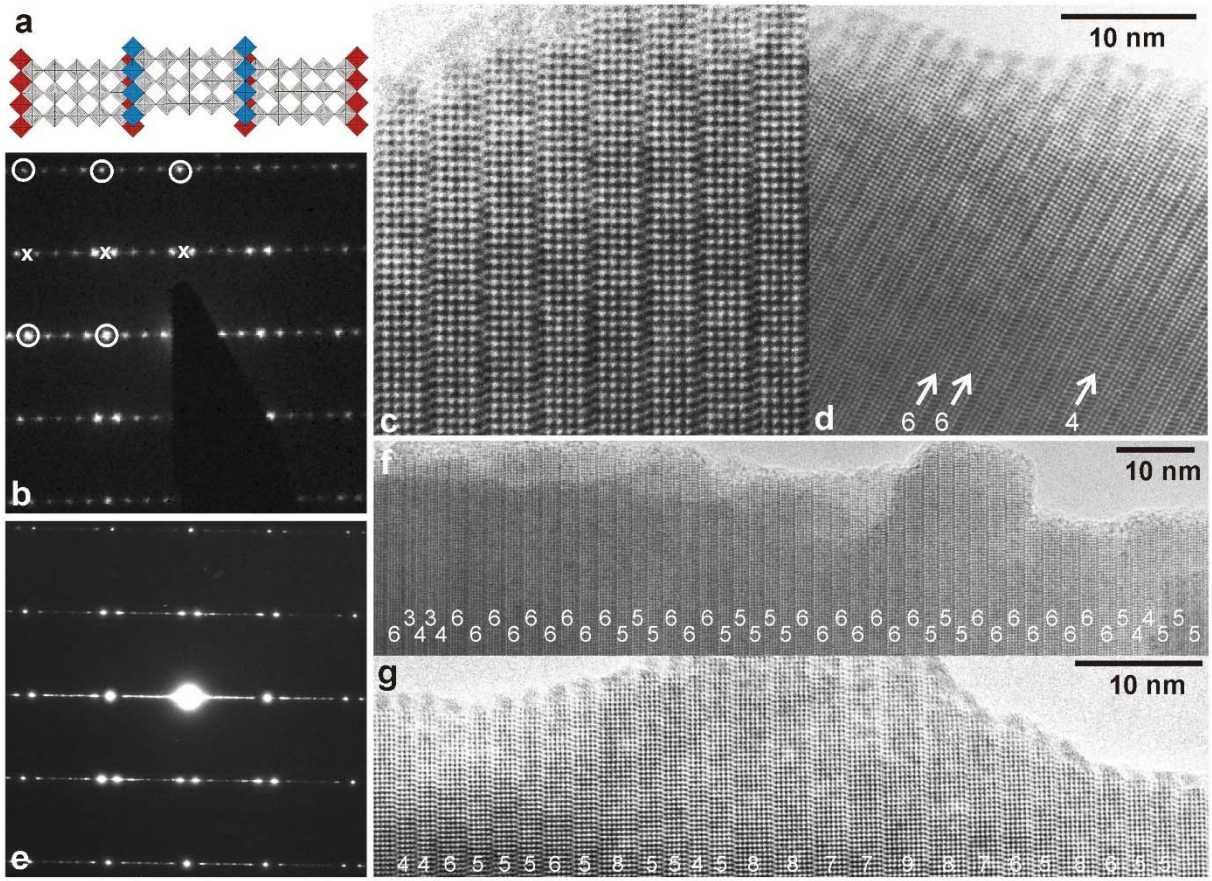

Figure 5.4: (a) Structural model for $Al_4W_{10}O_{32}$. (b) SAED pattern of a well-ordered domain with the fourfold superstructure. Some reflections of the basic ReO_3 structure are encircled, extinct ones marked by x. (c) HRTEM image of a perfectly ordered area. (d) HRTEM image of an area with inclusion of different slab width. (e) SAED pattern of a highly disordered crystal showing diffuse scattering between the reflections of the basic structure. HRTEM images of an intergrowth of the five and six octahedra wide slabs (f) and a disordered area with many different slab width.

5.2.3 Modulated Structures

The modulation of a basic structure can have different reasons: (i) Displacement: Atoms are displaced from the positions in the basic structure in a periodic way. (ii) Occupation: Empty positions are occupied or filled positions are occupied by two or more elements in a regular way. A commensurate modulation gives superstructure reflections besides that of the basic structure. An example is the structure of $Nb_8W_9O_{47}$ that is a threefold superstructure of the basic TTB type caused by the systematic occupation of 1/3 of the pentagonal channel by M-O strings (Fig. 5.1a).

A systematic investigation of the binary system Yb/Si uncovered the phase $YbSi_{1.4}$ crystallizing in an orthorhombic unit cell according to XRD investigations (a = 4.16, b = 23.5,

c = 3.78 Å; SPG: *Cmcm*).[44] The structure contains building blocks with three sheets of trigonal Yb_6 prisms that are connected to each other by face-sharing (Fig. 5.5). Two of these prism sheets are fully occupied by Si whereas the middle one is occupied by ca. 80 % only. This value was obtained from the electron density distribution by XRD. SAED and HRTEM investigations of several crystallites revealed the presence of two distinct ordering variants.

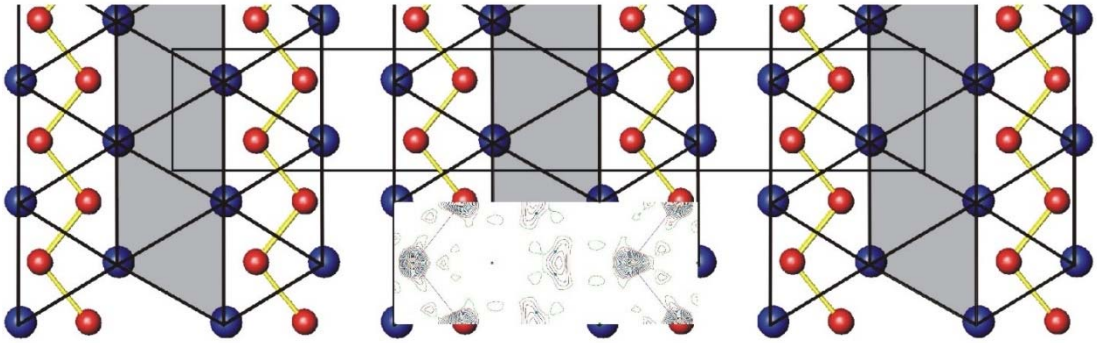

Figure 5.5: Structural model of the basic $YbSi_{1.4}$ structure along [001]. The Si positions in the grey areas are fully occupied in two columns while they are partially occupied the middle one. The electron density map (inset) shows a banana-like feature in the center that can be approximated by two split positions.

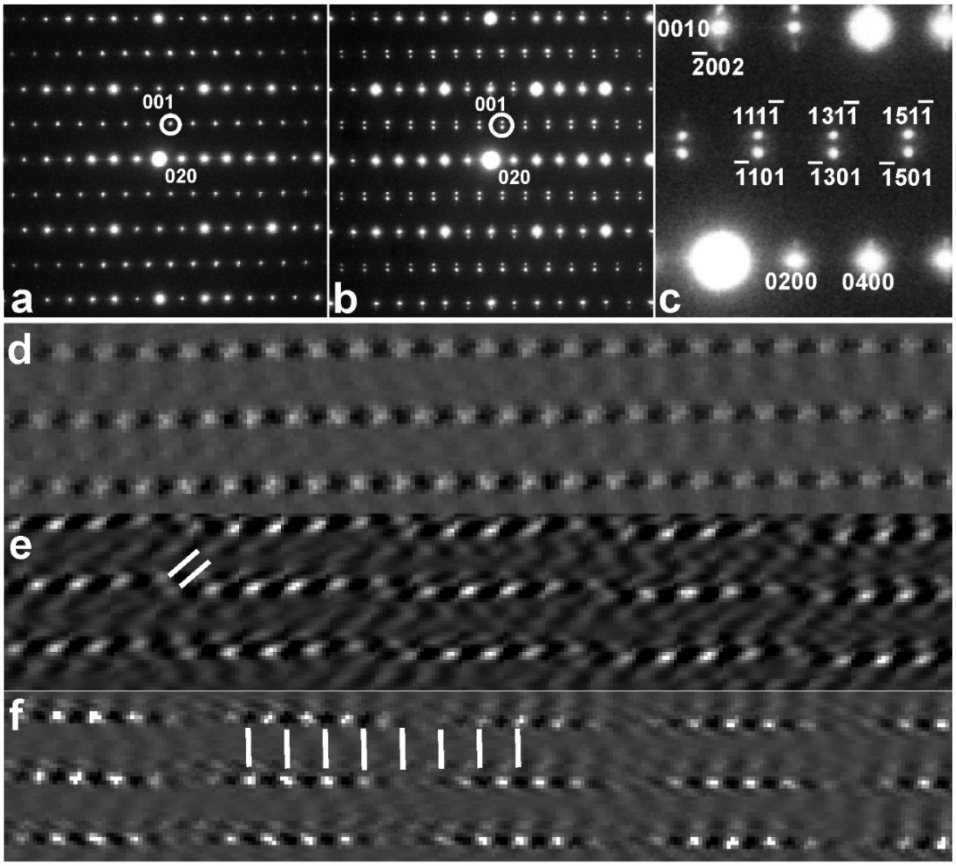

Figure 5.6: SAED patterns of $YbSi_{1.4}$_I (a) and $YbSi_{1.4}$_II (b),(c). Inverse Fourier transforms calculated from the HRTEM images using the superstructure reflections corresponding to the circles in (a) and (b), respectively. (d) Superstructure of $YbSi_{1.4}$_I. (e),(f) Two variants of incommensurately modulated structure in $YbSi_{1.4}$_II. The lines indicate the shift of adjacent domains with respect to each other.

[44] C. Kubata, F. Krumeich, M. Wörle, R. Nesper. The real structure of $YbSi_{1.4}$ - commensurately and incommensurately modulated silicon substructures. *Z. anorg. allg. Chem.* **631** (2005) 546-555.

The electron diffraction pattern of $YbSi_{1.4}$_I shows additional reflections (encircled in Fig. 5.6a) that indicate a unit cell with a doubled volume compared to the basic structure and the presence of a body-centering ($a_I = a = 4.16$, $b_I = 2$ x $c = 7.56$, $c_I = b = 23.51$ Å; SG *Imm*2). In the structural model derived from HRTEM images, Si fills 3/4 of the partly occupied Yb_6 prisms in a regular way (Fig. 5.6d).

In $YbSi_{1.4}$_II, the additional reflection is split into two (encircled in Fig. 5.6b). This points to an incommensurate modulation that required a four-dimensional diffraction vector for indexing all reflections: $\mathbf{H} = h\mathbf{a}^* + k\mathbf{b}^* + l\mathbf{c}^* + m\mathbf{q}$. The symmetry can be described in the 3+1 dimensional superspace group *Cmcm*(10γ). The evaluation of HRTEM images of $YbSi_{1.4}$_II by Fourier analysis revealed parallel domains with the structure of YbSi1.4_I that are shifted with respect to each other causing the modulation (Fig. 5.6e,f).

5.2.4 Dodecagonal Quasicrystals

The characteristic of a quasicrystal is the presence of long-range orientational order leading to sharp reflections in the diffraction patterns but the absence of translational symmetry. Besides the icosahedral quasicrystals like the AlMn phase discovered by *Shechtman*, there are two-dimensional ones that exhibit 8, 10, or 12-fold symmetric diffraction pattern when observed along the periodic axis.[45] Such kinds of symmetry are forbidden in classical crystallography.

The first chalcogenide quasicrystal was discovered in the system Ta-Te.[46] It is one of the few examples of dodecagonal quasicrystals that are distinguished by the presence of twelvefold rotational symmetry in the diffraction patterns. Remarkably, there are several phases in the systems Ta-Te and Ta-V-Te that are structurally closely related as evident from the common positions of the main peaks in the electron diffraction patterns (Fig. 5.7). The reflections in the dodecagonal phase dd-$(Ta,V)_{1.6}Te$ show rotational by no translation symmetry. In the related phases, so-called approximants, superstructure reflections appear besides the main reflections.

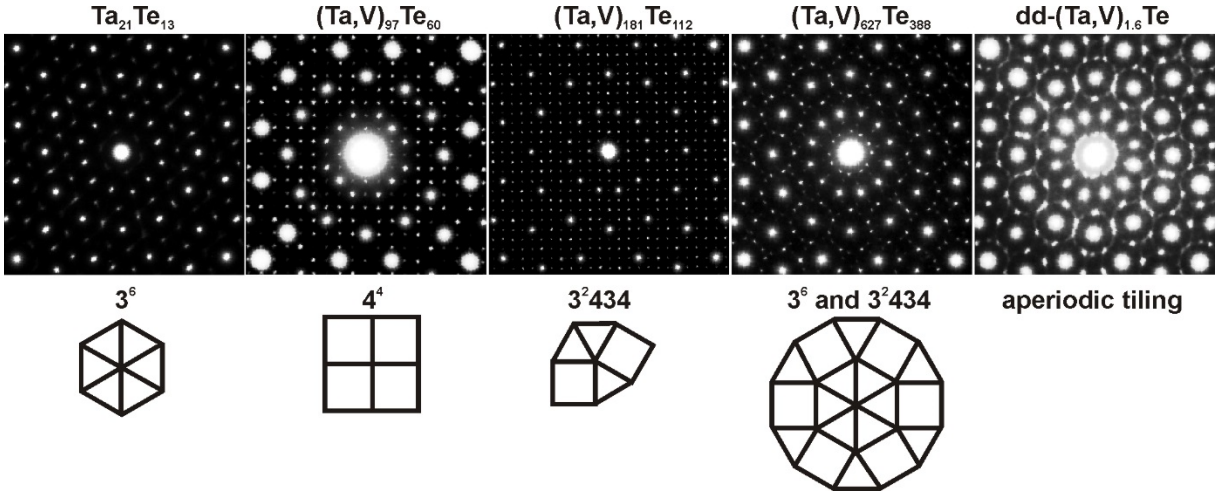

Figure 5.7: Electron diffraction patterns of the different phases found in the systems Ta-Te and Ta-V-Te with the scheme of the corresponding vertex configuration.

[45] W. Steurer. Why are quasicrystals quasiperiodic? *Chem. Soc. Rev.* **41** (2012) 6719–6729.

[46] (a) M. Conrad, F. Krumeich, B. Harbrecht. A dodecagonal quasicrystalline chalcogenide. *Angew. Chem. Int. Ed.* **37** (1998) 1383-1386. (b) F. Krumeich, M. Conrad, H.-U. Nissen, B. Harbrecht. The mesoscopic structure of disordered dodecagonal tantalum telluride: a high-resolution transmission electron microscopy study. *Phil. Mag. Letters* **78** (1998) 357-367.

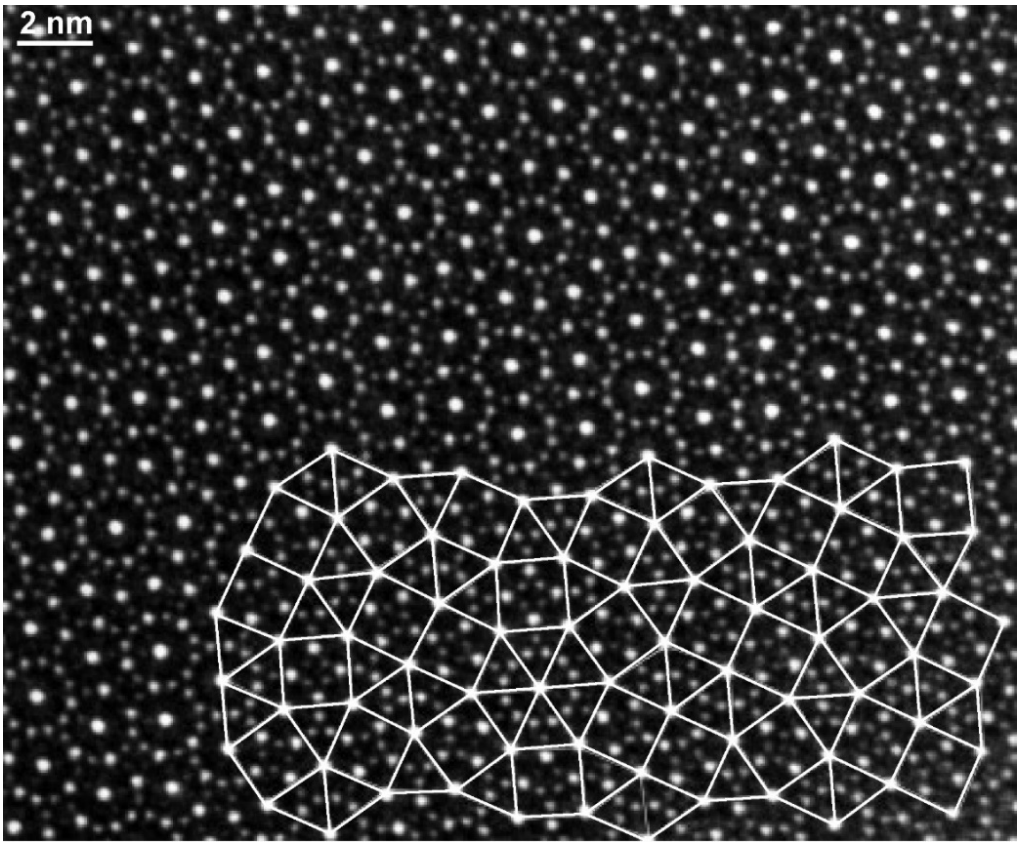

Figure 5.8: HRTEM of dodecagonal (Ta,V)$Te_{1.6}$. The array of bright dots is described by an aperiodic square-triangle tiling.

The HRTEM image of dd-$(Ta,V)_{1.6}Te$ recorded along the periodic direction demonstrates the absence of translation symmetry in the quasicrystalline plane (Fig. 5.8). There are repeated units consisting of twelve-rings of bright dots centered by brighter ones. Seemingly, these units are randomly arranged. A close examination reveals that these units are in fact located on the vertices of a square-triangle tiling with an edge length of ca. 2 nm. In contrast to the aperiodic tiling found for the dodecagonal phase, these units are ordered on regular tilings in case of the rational approximants (Fig. 5.7 bottom). In the simplest cases, only triangles (vertex configuration 3^6) or squares appear (4^4).

To suggest a structural model for the atomic arrangement of a quasicrystal, it is essential to uncover the structure of an approximant phase. Here, the structure of $Ta_{97}Te_{60}$ was solved using X-ray single crystal data.[47] $Ta_{97}Te_{60}$ consists of basic $Ta_{151}Te_{74}$ cluster (Fig. 5.9a). The cluster centers are located on the vertices of a square lattice with an edge length of 1.94 nm (Fig. 5.9b). HRTEM images of this phase recorded at different defocus values reveal the arrangement of the basic cluster on a regular square tiling (Fig. 5.10). Simulated images were calculated taking the imaging properties of the microscope and the structural data for this phase into account. Close to Scherzer defocus (Fig. 5.10a), the atomic sites are imaged with dark contrast giving rise to a rather complicated contrast pattern reflecting the crystal potential. At Δf = -80 nm (Fig. 5.10a), the cluster appears as a bright dot surrounded by two concentric rings of twelve bright

[47] B. Harbrecht, M. Conrad. $Ta_{97}Te_{60}$: A crystalline approximant of a tantalum telluride quasicrystal with twelvefold rotational symmetry. *Chem. Eur. J.* **8** (2002) 3093–3102.

dots. At a high defocus Δf = -180 nm, there is only one of the concentric rings left. However, this image with reduced information already defines the position of the cluster clearly and this focus has been used to record the HRTEM image of the dodecagonal phase (Fig. 5.8). The structure at each vertex position of the square-triangle tiling thus corresponds to a $Ta_{151}Te_{74}$ cluster.

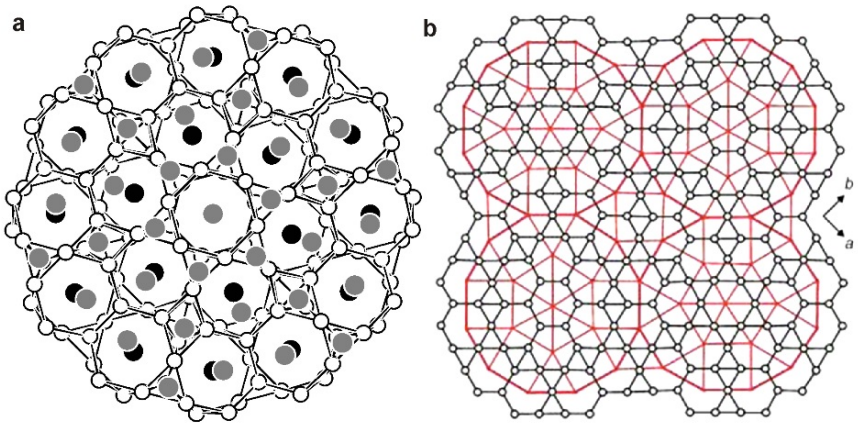

Figure 5.9: (a) Structure of a $(Ta,V)_{151}Te_{74}$ cluster. (b) Square array of these clusters as present in $Ta_{97}Te_{60}$.

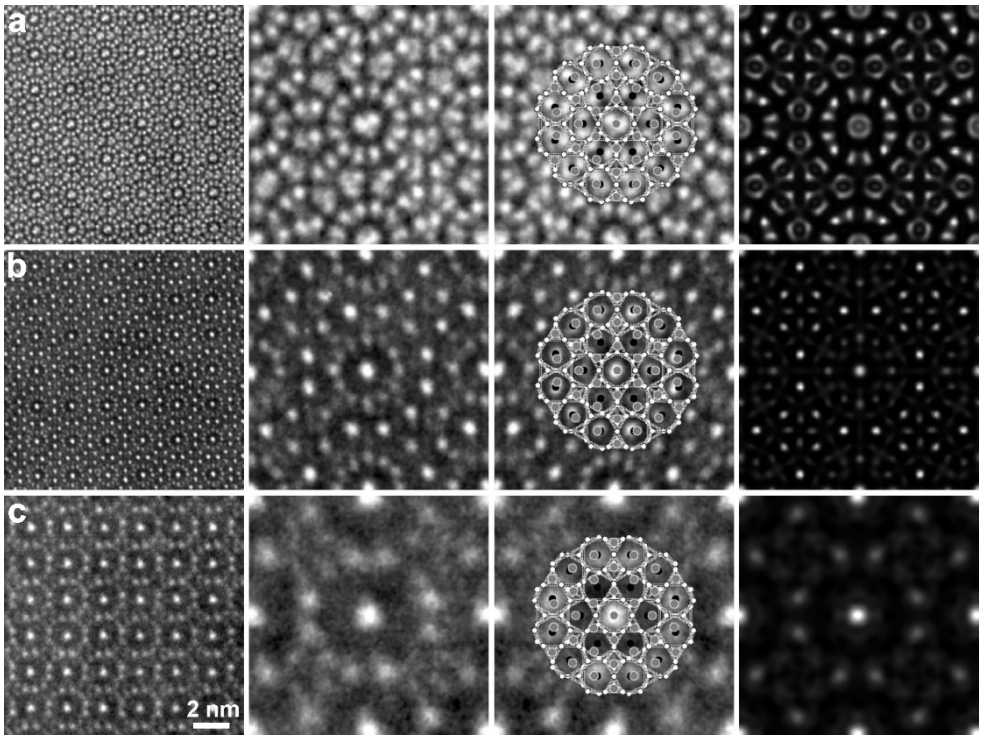

Figure 5.10: HRTEM images of the same area of $Ta_{97}Te_{60}$ recorded at three different defocus values (first column). The structural model of the $Ta_{151}Te_{74}$ cluster is fitted into a magnification of the corresponding HRTEM image. The right columns shows simulations: (a) defocus Δf = -50 nm; (b) Δf = -80 nm; (c) Δf = -180 nm.

Arranging square and triangles gives rise to numerous possibilities to cover the plane with periodic and aperiodic arrays (cf. Fig. 5.7 bottom). This flexible structural principle underlying the Ta-V-Te phases favors their frequent intergrowth and the formation of defective arrays that can be regarded as intermediate states of order between the crystalline approximants and the

quasicrystalline phase. An example is reproduced in Fig. 5.11: in this area, alternating slabs of triangles and squares appear. Furthermore, the width of the individual triangle slabs varies from one to four triangles. However, the assignment of squares and triangles to the HRTEM is sometime ambiguous. Arrows in Fig. 5.11 mark a peculiar contrast motif that corresponds to 30° rhombs. However, such a structural feature is not compatible with the building principle of these phases. In fact, the observation of such rhombs points to stacking faults in direction of observation (overlap of squares and triangles) as image simulations with corresponding structural models could verify.[48]

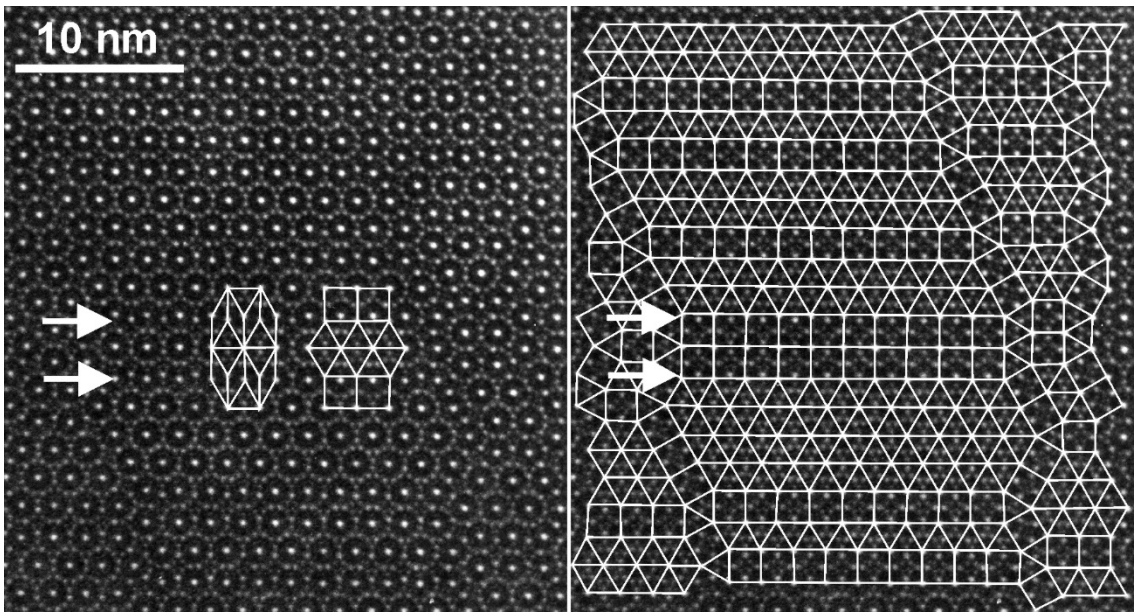

Figure 5.11: HRTEM image of partly ordered tantalum telluride with alternating slabs of squares and triangles. Their position is unclear in the slab indicated by arrows.

5.3 In-Situ Studies

TEM investigation are usually carried out in high vacuum at room temperature. Special holders allow to perform different experiments like straining tests or electrical measurements. Even chemical experiments are possible inside the microscope today: the electron beam interacts with gas or even liquid phase present in thin layers while the high vacuum is maintained in the rest of the microscope column (see 5.3.3). The temperature can be changed either by cooling down or heating up the sample. Cooling beam sensitive samples is often the only possibility to investigate them. The most important example are biological object; different cryo-methods are used for their characterization. Phase changes and transitions that occur at elevated temperature can be observed by heating up a sample. A few examples and further aspects are discussed in the following.

[48] F. Krumeich, C. Reich, M. Conrad, B. Harbrecht. Periodic and aperiodic arrangements of dodecagonal $(Ta,V)_{151}Te_{74}$ clusters studied by transmission electron microscopy - The method's merits and limitations. *Mater. Sci. Eng.* **294–296** (2000) 152–155.

5.3.1 Heating Experiments

Carbon-coated $LiFePO_4$ is a promising material for battery applications. On one hand, the carbon increases the electric conductivity of the electrochemically active but poorly conducting $LiFePO_4$ and, on the other hand, the coating protects the core from reaction with the electrolyte. The material investigated here was prepared by flame spray pyrolysis. It shows an interesting thermal behavior that has been studied *in-situ* in the TEM.[49] A carbon shell of a few nm thickness covers the $LiFePO_4$ nanoparticles (diameter ca. 10-50 nm, Fig. 5.12a). Drastic structural changes happen at temperatures above 700°C, when LiFePO4 forms large particles and leaves back hollow carbon cages (Fig. 5.12).

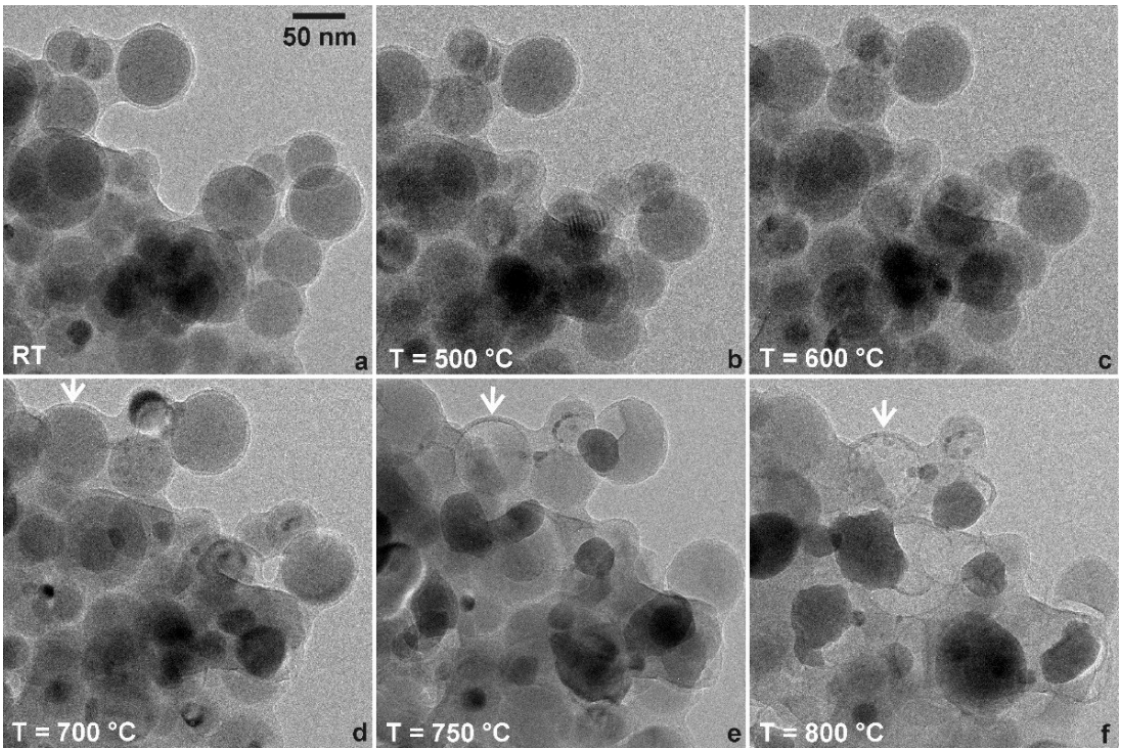

Figure 5.12: TEM images of the same area of the carbon-coated $LiFePO_4$ at room temperature (a) and after different stages of the in-situ heating experiment (b-f). Most changes − in particular the formation of empty carbon shells (an example is marked by arrows) and the particle growth − only occur at temperatures above 700 °C (d-f).

5.3.2 Cooling Experiments

Cooling can efficiently protect beam sensitive specimens. A current research topic are perovskite-type lead halides that are semiconductors with a narrow band gap and show bright photoluminescence making them attractive for several applications.[50] The electron microscopy investigation of these phases is impeded by their decomposition in the electron beam. Dark dots appear in the TEM images, bright ones in the HAADF-STEM images, indicating the formation of lead particles (Fig. 5.13a). This segregation effect does not occur if the sample is mounted

[49] F. Krumeich, O. Waser, S. E. Pratsinis. Thermal annealing dynamics of carbon-coated $LiFePO_4$ nanoparticles studied by in-situ analysis. *J. Solid State Chem.* **242** (2016) 96–102.

[50] M. V. Kovalenko, L. Protesescu, M. I. Bodnarchuk. Properties and potential optoelectronic applications of lead halide perovskite nanocrystals. *Science* **358** (2017)745–750.

on cooling holder working with liquid nitrogen (Fig. 5.13b). Then, the investigation is carried out at T ≈ -172 °C.

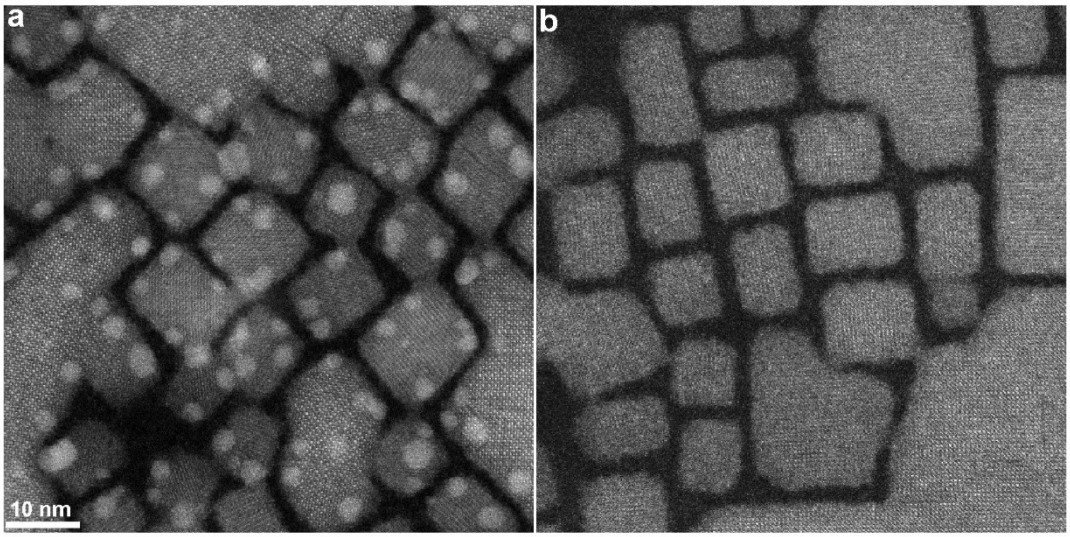

Figure 5.13: HAADF-STEM images of a lead halide recorded at room temperature (a) and at liquid nitrogen temperature (b).

5.3.3 Chemistry inside the TEM

For the electron microscopy characterization of the outcome of chemical reactions, the starting material and the reaction products are usually investigated separately with the reaction itself carried out *ex-situ*. Many insights into structural modifications during chemical reactions have been gained by such studies. However, the question always remains whether the results obtained from such observations in high vacuum are really representative. An approach to solve this problem and to observe solid-gas reactions *in-situ* is to allow a small amount of gas in the specimen area. While the sample should be fully immersed in the gas, the thickness of this gas layer must be small to minimize unspecific scattering of the electron beam as this decreases the resolution of the TEM. Two different experimental concepts to achieve this goal are implemented in modern transmission electron microscopes:

(i) **Differential pumping**. Gas is let into the specimen area while the high vacuum other sections of the microscope is maintained. Additional apertures separate this area from the rest of the microscope column and additional pumps remove the gas close to the specimen. Such dedicated microscopes equipped with differential pumping stages are designated as environmental TEMs (ETEMS).[51]

(ii) **Closed cells**. The sample is placed between two electron-transparent windows consisting of a thin film (≤ 40 nm) of light element materials (e.g. SiC, SiN or graphene). The special construction of the specimen holder allows one or more gases to pass through the space between

[51] (a) E. D. Boyes, P. L. Gai. Environmental high resolution electron microscopy and applications to chemical science. *Ultramicroscopy* **67** (1997) 219-232. (b) J. R. Jinschek, Advances in the environmental transmission electron microscope (ETEM) for nanoscale in situ studies of gas–solid interactions. *Chem. Commun.* **50** (2014) 2696-2706.

the windows to interact with the material. If MEMS chips act as sample carriers, they can be heated up by an electric current.[52]

With these experimental set-ups, it is possible to perform and observe solid-gas reactions inside the TEM. The resolution capability of the microscope is of course reduced in both cases by scattering processes. By using microscopes equipped with a C_s corrector, it is nevertheless possible to achieve high resolution even under such adverse conditions. This combination of environmental options and aberration correction together with fast cameras enables one to observe solid-gas reactions in a TEM. Even the observation of reactions in liquids are possible today using MEMS-based holders that contain the liquids between two membranes.[53] These approachs are certainly steps forward to a chemical lab working inside transmission electron microscopes mimicking real world conditions.[54]

[52] R. Ramachandramoorthy, R. Bernal, H. D. Espinosa. Pushing the envelope of in situ transmission electron microscopy. *ACS Nano* **9** (2015) 4675–4685.

[53] B. H. Kim, J. Yang, D. Lee, B. K. Choi, T. Hyeon, J. Park. Liquid-phase transmission electron microscopy for studying colloidal inorganic nanoparticles. *Adv. Mater.* **30** (2018) 1703316.

[54] (a) J. F. Creemer, S. Helveg, G. H. Hoveling, S. Ullmann, A. M. Molenbroek, P. M. Sarro, H. W. Zandbergen. Atomic-scale electron microscopy at ambient pressure. *Ultramicroscopy* **108** (2008) 993–998. (b) J. Wu, H. Shan, W. Chen, X. Gu, P. Tao, C. Song, W. Shang, T. Deng. In situ environmental TEM in imaging gas and liquid phase chemical reactions for materials research. *Adv. Mater.* **28** (2016) 9686–9712.

6 Conclusions

Electron microscopy methods are of high value for materials science as they provide indispensable information in the course of a comprehensive characterization of materials that other analytical tools often cannot provide. Modern electron microscopy comprises a wide range of different advanced methods that use the various signals resulting from the multitude of interactions of the electron beam with the sample. These methods are able to characterize the structure, morphology and composition with high lateral resolution. In this contribution, only the most important and versatile TEM-based techniques widely applied for the investigation of inorganic solid materials have been treated and illustrated by selected examples from various research projects in solid state chemistry. The type of specimens that can be observed is very broad and includes inorganic and organic materials, biological objects as well as composite structures. Thus, the impact of electron microscopy on many fields of natural sciences is immense.

Acknowledgements:

Most TEM and STEM images discussed in this contribution were recorded in the course of investigations performed for different research groups at ETH Zürich. The microscopes of the Scientific Center for Optical and Electron Microscopy (ScopeM)[55] were used for these studies. ScopeM is gratefully acknowledged for providing generous measuring time and technical support.

[55] Website: www.scopem.ethz.ch